

Speckle Suppression by Decoherence in Fluctuation Electron Microscopy

Aram Rezikyan,^{1,*} Zechariah J. Jibben,² Bryan A. Rock,¹ Gongpu Zhao,³ Franz A.M. Koeck,¹ Robert F. Nemanich,¹ and Michael M.J. Treacy¹

¹Department of Physics, Arizona State University, Tempe, AZ 85287, USA

²Ira A. Fulton School of Engineering, Arizona State University, Tempe, AZ 85287, USA

³Department of Structural Biology, University of Pittsburgh School of Medicine, Pittsburgh, PA 15260, USA

Abstract: We compare experimental fluctuation electron microscopy (FEM) speckle data with electron diffraction simulations for thin amorphous carbon and silicon samples. We find that the experimental speckle intensity variance is generally more than an order of magnitude lower than kinematical scattering theory predicts for spatially coherent illumination.

We hypothesize that decoherence, which randomizes the phase relationship between scattered waves, is responsible for the anomaly. Specifically, *displacement decoherence* can contribute strongly to speckle suppression, particularly at higher beam energies. Displacement decoherence arises when the local structure is rearranged significantly by interactions with the beam during the exposure. Such motions cause diffraction speckle to twinkle, some of it at observable time scales.

We also find that the continuous random network model of amorphous silicon can explain the experimental variance data if displacement decoherence and multiple scattering is included in the modeling. This may resolve the longstanding discrepancy between X-ray and electron diffraction studies of radial distribution functions, and conclusions reached from previous FEM studies.

Decoherence likely affects all quantitative electron imaging and diffraction studies. It likely contributes to the so-called Stobbs factor, where high-resolution atomic-column image intensities are anomalously lower than predicted by a similar factor to that observed here.

Key words: Fluctuation electron microscopy, decoherence, continuous random network, medium-range order, amorphous materials

INTRODUCTION

Fluctuation electron microscopy (FEM) examines the statistics of spatially resolved electron diffraction intensity to reveal medium-range order (MRO) in amorphous materials (Treacy & Gibson, 1996; Gibson & Treacy, 1997; Voyles & Abelson, 2003; Treacy, 2005; Treacy et al., 2005; Lee et al., 2010). FEM has been used to study MRO in amorphous Si and Ge (Treacy & Gibson, 1996; Gibson & Treacy, 1997; Gibson et al., 1998, 2010; Treacy et al., 1998; Voyles et al., 2001; Bogle et al., 2007), and to infer structural details of metallic glasses (Li et al., 2001, 2003; Stratton et al., 2005; Wen et al., 2009), oxide framework glasses (Cheng et al., 2004; Zhao et al., 2010), and amorphous carbons (Chen et al., 2004; Liu et al., 2007; Zhao et al., 2009).

High-resolution imaging in the transmission electron microscope (TEM), or the scanning transmission electron microscope (STEM), generally fails to resolve atomic structure in amorphous materials because images are a projection through many tens, or even hundreds, of atoms (Howie, 1978). Unlike in crystals, where atoms line up in columns along the

principal crystallographic directions revealing periodicity, amorphous materials do not contain significant atomic alignments unless there is MRO present. The occurrence of periodic patterns in high-resolution images of disordered materials is often illusory (Treacy et al., 2005). However, with care, and by using a statistical approach, some successes have been reported (Chen et al., 2002; Cheng et al., 2002).

On the other hand, high-resolution X-ray, neutron, and electron diffraction studies give quantitative radial distribution functions (RDFs), which provide useful generalizations about sample averages (Laaziri et al., 1999; McBride & Cockayne, 2003; Cockayne, 2007). Since diffraction data are spatially unresolved sample averages, it is harder to infer details about structural inhomogeneity and its length scale. RDFs obtained by diffraction provide important short-range information, such as nearest-neighbor coordination number and bond distance, but are less sensitive to the presence of MRO. It has been shown that models with and without MRO can reproduce the RDF data (Treacy & Borisenko, 2012a, 2012b). Small-angle X-ray scattering can detect density fluctuations in materials at nanometer length scales (Xie et al., 2013), but cannot tell us much about the structural details that cause them.

It has been long appreciated within the microscopy community that a judicious combination of imaging and

Received January 24, 2015; accepted August 11, 2015

*Corresponding author. arezikya@hotmail.com

diffraction methods can potentially reveal more information about MRO than either technique on its own (Howie et al., 1973; Gibson, 1978; Gibson & Howie, 1978; Fan & Cowley, 1985, 1988; Howie et al., 1985; Rodenburg, 1988). However, difficulties in collecting large amounts of quantitative, spatially resolved, diffraction data limited the scope of this approach. The advent of charge-coupled device (CCD) cameras for electron microscopy in the early 1990s, in conjunction with advances in computing technology, spurred progress leading to the FEM technique. Important outstanding issues remain, however; the inherent complexity of the data makes it difficult to extract a characteristic structure; there are puzzling discrepancies between experimental data and kinematical diffraction theory. Consequently, the FEM technique to date has remained semiquantitative.

In essence, FEM examines the mean and the normalized variance of diffracted intensity from many small sample volumes, plotted as a function of diffraction vector. Diffraction, as a function of position in an amorphous sample, is inherently speckled, and it is the variation of these fluctuations in intensity that is explored. The normalized variance of intensity as a function of scattering vector (k_x, k_y) , reveals these fluctuations, obtained as

$$V(k_x, k_y; R) = \frac{\langle I^2 \rangle_r(k_x, k_y; R)}{\langle I \rangle_r^2(k_x, k_y; R)} - 1. \quad (1)$$

The variance depends on the width of the probed regions, which is controlled by the nominal probe resolution, R . As the variance is proportional to the second moment of diffraction intensity, it is influenced by four-body (i.e., pair-pair) correlations in the sample structure. Inversion of such data, to obtain the nonperiodic structure, is significantly more difficult than it is for inverting two-body (i.e., pair-correlated) mean diffraction data from crystals (Treacy & Gibson, 1996). Nevertheless, FEM data show compellingly, albeit qualitatively, that MRO is present in some disordered materials. The likely form of the MRO is usually deduced by comparing data with simulations from a set of possible models. Variance peak location and *relative* peak heights are used for matching models. However, it has been unclear why experimental normalized variance is generally one to two orders of magnitude smaller than calculated. Uncontrolled experimental conditions, such as illumination incoherence, specimens thickness, or models being overly simplified, were possible explanations.

FEM represents a compromise; it sacrifices high spatial resolution and high reciprocal space resolution to allow an exploration of diffraction variations between small volumes across the sample. The length scale being probed is determined by the image resolution or probe size, which for maximum sensitivity should be comparable with the characteristic length scale of the MRO.

Quantitative analysis of FEM data has been problematic. Simulated annealing has been used to invert FEM data to obtain a representation of inhomogeneous structures (Biswas et al., 2005; Hwang et al., 2009; Borisenko et al., 2012; Treacy & Borisenko, 2012a, 2012b). Mean diffraction data and the normalized variance (variance divided by the square

of the mean, as in equation 1) of speckle intensities are used as constraints. A cost function is used that depends quadratically on the difference between data and kinematical diffraction simulations, as well as on an empirical potential that asserts chemical reasonableness. Atoms are moved in an attempt to minimize the cost function using the Metropolis algorithm (Press et al., 1992). Since the computed variance as a function of scattering vector is always significantly higher than the experimental variance, an empirical multiplicative factor is introduced so that the areas under the normalized variance curves match. This introduces an additional refinement parameter, the structural meaning of which was not understood.

There are two modalities of FEM, related to each other via the reciprocity principle. In one, tilted dark-field images are collected as a function of illumination tilt vector q . Here, we refer to this as the dark-field FEM (DFFEM) method. The STEM-equivalent mode collects a series of diffraction patterns as a function of probe location, the scanning transmission fluctuation electron microscopy (STFEM) mode. In principle, for a given resolution R , each mode collects a four-dimensional set of diffraction data; $I(x, y; q_x, q_y; R)$ for DFFEM, and $I(x, y; k_x, k_y; R)$ for STFEM, where $(q_x, q_y) \equiv -(k_x, k_y)$. In practice, DFFEM undersamples the (q_x, q_y) space and STFEM undersamples the (x, y) space. Consequently, in STFEM, each sampled region tends to receive a much higher electron fluence than it does in DFFEM. This can be an important distinction between the two FEM methods.

Illumination coherence is an important parameter in FEM. The earliest form of FEM was referred to as *variable coherence microscopy* (Treacy & Gibson, 1996). The idea was that the spatial coherence volume around each atom could be adjusted by modifying the electron illumination conditions. In particular, the narrow coherence volume associated with hollow-cone illumination had the desirable effect of filtering the coherent interferences so that the main contribution to speckle is from those neighboring atoms that line up closely in columns along the optic axis. It is attuned better to small crystallites if present within the disordered matrix. Speckle arising from interference between structurally distant atoms, which can be considered to be structural noise as far as MRO is concerned, would be suppressed. Experimentally, this idea seemed to work; hollow-cone illumination does suppress speckle strongly, generally by about four orders of magnitude relative to coherent kinematical theory.

FEM experiments conducted using single-tilt dark-field imaging, the DFFEM modality, which produces an extensive periodic coherence volume, suppresses speckle also. Although the speckle variance from single-tilt illumination is generally two orders of magnitude higher than that for hollow cone, because the effective coherence volume is larger, it is still more than an order of magnitude lower than kinematical theory predicts. In theory, tilted dark-field illumination should not offer any significant advantage over hollow-cone illumination for distinguishing MRO-related speckle from noise-related speckle. Experimentally, the main outcome from using tilted dark-field illumination was to amplify the overall variance pattern, with minor

influence on peak shapes and relative heights. The fact that normalized speckle variance in FEM is about an order of magnitude lower than kinematical theory predicts for fully coherent illumination, has been a longstanding puzzle.

In this report, we present experimental and modeling evidence to show that *decoherence* (Howie, 2011) during the electron-scattering process is surprisingly large, and is an important contributor to speckle suppression. Speckle statistics show that, to some extent, decoherence mimics the role of spatial incoherence, which is probably why its contribution was not recognized earlier. We conclude that an important source of decoherence arises from structural changes within the sample under the influence of the beam during the data collection process. We refer to this effect as *displacement decoherence*. Atomic motions alter the interferences between scattered waves causing speckle to twinkle, some of it at visible time scales, 10 ms and above. This decoherence is similar to the diffuse scattering that arises from atomic thermal motion, but it is not a thermal process, and the time scales involved are determined by the fluence rate of the beam. It is a distinct decoherence mechanism from those considered by Howie (2011).

Although this paper concerns itself mainly with diffraction speckle, it is clear from our results that the decoherence we observe will be an important issue for all quantitative studies of electron imaging and diffraction. It likely plays a role in explaining why electron ptychography at high electron energies does not perform as well as the X-ray or optical counterparts (Rodenburg, 2008; Kamimura et al., 2010; Humphry et al., 2012). It provides, undoubtedly, a significant contribution to the so-called “Stobbs factor,” where experimental high-resolution lattice image intensities are significantly lower than predicted (Hýtch & Stobbs, 1994; Boothroyd, 1998).

EXPERIMENTAL AND COMPUTATIONAL DETAILS

Amorphous Samples

FEM results reported here were carried out using two TEMs. Tilted DFFEM studies were carried out on a JEOL (Peabody, MA, USA) 2010F equipped with a Schottky field-emission gun operated at 200 kV. Images were collected on a Gatan (Pleasanton, CA, USA) MSCTM 794 CCD camera. The 10- μm -diameter objective aperture ($Q \approx 1.2 \text{ nm}^{-1}$) generated a nominal resolution $R \approx 1.0 \text{ nm}$ at 200 kV ($\lambda = 2.51 \text{ pm}$). At magnifications of 40,000 \times , images were sampled at about $\sim 0.5 \text{ nm/pixel}$. Scans from several different sample regions were made to ensure representative data. Tilted dark-field image exposure times were adjusted so that regions of interest averaged ~ 100 counts/pixel. This is usually sufficient to keep the variance contributions from shot noise at a low level. As carbon is a weak scatterer, higher counts, requiring longer exposure times, were avoided so that sample drift did not affect results. Nevertheless, images taken at higher scattering vectors required longer exposure times, up to 50 s at

$q = 10 \text{ nm}^{-1}$. The specimen and holder were generally allowed to stabilize for about 30–60 min after insertion into the microscope until observable drift rates were low. The longest exposures were the most vulnerable to drift, rendering the speckle in DFFEM image data as short parallel streaks along the drift direction. Variance data at tilts above $q > 8 \text{ nm}^{-1}$ are the most vulnerable to drift and shot noise.

The scanning probe, STFEM, studies were carried out in the NBD-S mode on a JEOL (Peabody, MA, USA) ARM200F equipped with a Schottky field-emission gun operated at 80 or 200 kV. Diffraction patterns were collected on a Gatan (Pleasanton, CA, USA) 833 Orius SC200D CCD camera. The NBD-S mode condenser system gave a measured electron probe resolution of about 1.5 nm when using a 20 μm condenser lens (CL) aperture at 200 kV, and a resolution of 1.3 nm with a 30 μm aperture at 80 kV. The UNCD sample (described below) was studied at 80 keV, with a 20- μm CL aperture giving about 2 nm resolution. Another condenser configuration with a 10- μm CL aperture and higher excitation of the first CL was used for high spatial coherence FEM experiments with $R \approx 2.4 \text{ nm}$.

Probe instabilities in NBD-S mode were measured by recording an image of the probe with no sample present. Over a 2-min observation period, excursions of the probe center were as large as 0.2 nm, tending to return to the nominal center position. Systematic probe drift is insignificant (less than 0.2 nm in 2 min). Given that the probe width is significantly more than 1 nm in our experiments, these instabilities are not expected to have a significant affect on nanobeam diffraction patterns.

Specimen drift was monitored by tracking the motion of notable fiducial sample features before and after data collection. For the DFFEM studies, drift is also revealed after the experiment by taking cross-correlations between successive images. This was found to work reliably even in the absence of visually obvious fiducial features in the images. For nanobeam diffraction data, collected in NBD-S mode, the probe had to be defocused to reveal the reference features. Drift rates needed to be sufficiently slow so that lateral specimen motion was significantly less than the nominal probe size over the exposure time. Typically, linear drift rates of less than 0.1 nm/s are required.

A Digital MicrographTH (Gatan, Pleasanton, CA, USA) script controlled the x and y beam deflectors, enabling probe positioning and data acquisition. Most data were collected from a 10×10 grid of points separated by about 7 nm on the sample. Exposure times were adjusted for each CL configuration and sample (ranging from 0.01 to 3.7 s) in order to minimize the shot noise contribution to the FEM data at higher k . The camera length was adjusted to collect data in the range $-14 \text{ nm}^{-1} < k < 14 \text{ nm}^{-1}$.

Experiments from three types of carbon, and one amorphous silicon sample, are presented here. Both the amorphous silicon and carbon are similar in that both form predominantly tetrahedral networks. In the amorphous state, typical Si–Si spacings are around 0.24 nm, and C–C spacings are around 0.15 nm. They have different beam

damage thresholds, with carbon being more sensitive to knock-on damage.

- (1) aC1: an amorphous carbon film, ~30 nm thick, prepared by vacuum-sputtering graphitized carbon rods onto mica. The carbon film was floated onto distilled water and collected on a 300 mesh 3-mm Cu grid.
- (2) aC2: a commercial, “ultrastable,” amorphous carbon film made by GloEMT™ Co. (Shanghai, China), supported on a 200 mesh 3 mm Cu grid. Its thickness, measured directly from a sideways view afforded by a curled-up region, was 30 ± 1 nm.
- (3) UNCD: a layer of ultrananocrystalline diamond carbon was synthesized by plasma-assisted chemical vapor deposition onto a 100-oriented single-crystal Si substrate (Sun et al., 2014). A cross-section sample was prepared by the focused ion beam lift-out technique, using an FEI Nova (Hillsboro, Oregon, USA) 200 NanoLab™ instrument with an Omniprobe™ (Oxford Instruments, Abingdon, Oxfordshire, UK) tip. Final ion beam thinning was done with $\sim 1^\circ$ scan rotation relative to the lifted-out sample, resulting in a wedge-shaped TEM sample with a $\sim 2^\circ$ wedge angle.
- (4) aSi: a freestanding a-Si sample, ~20 nm thick, was prepared by sputtering Si at 200°C onto an amorphous carbon film, which was lifted off onto a Cu grid. The sample was argon plasma cleaned to remove the carbon support film before observation. The structure of the a-Si film did not appear to have been affected by this cleaning. This, and similar samples, were used in previous FEM studies, and are typical of paracrystalline amorphous silicon (Gibson et al., 2010).

These four samples were chosen because they represent “canonical” FEM samples, and are familiar to most practitioners of FEM. In particular, amorphous silicon has been studied extensively using FEM by several authors (Treacy & Gibson, 1996; Gibson & Treacy, 1997; Gibson et al., 1998, 2010; Voyles et al., 2001; Bogle et al., 2007; Borisenko et al., 2012; Treacy & Borisenko, 2012a, 2012b). Carbon and silicon are compared because carbon, having a lower atomic mass ($A_C \approx 12$) than silicon ($A_{Si} \approx 28$), has a lower beam energy threshold for knock-on damage, allowing us to compare the effects of beam energy on FEM variance. The UNCD was of interest because it exhibits clear long-range order at length scales of 2–10 nm, just beyond the MRO length scales of ~ 0.5 – 2.0 nm. This allows us to explore the relative effect of decoherence on variance peaks relative to the variance background (between the peaks).

Computational Details

We present computational results for three structurally distinct models of tetrahedral silicon. All models were periodic with a large unit cell, within which atoms were aperiodic.

- (1) Random: the first model is for a random distribution of 4,096 Si atoms within a periodic cubic cell of edge length 4.524 nm. The atomic x, y, z locations were determined

by a random number generator that sampled the unit cell volume uniformly. There are no bond distance or bond angle constraints, and the RDF is essentially flat.

- (2) Continuous random networks (CRN1 and CRN2): a second model type is the periodic CRN. Two models are used. The first, CRN1, was constructed by Wooten et al. (1985). This also has 4,096 Si atoms within the same periodic cubic cell of edge length 4.524 nm. In this model, Si atoms obey reasonable chemical constraints with four Si–Si bonds per Si atom arranged in an approximately regular tetrahedral fashion, with Si–Si distances near 0.24 nm. A second model, CRN2, was constructed by Barkema & Mousseau (2000), and has 100,000 Si atoms in a cubic cell of edge length 12.405 nm. This latter model was used when greater thickness was needed. Both CRN models exhibit a good match to experimental RDF data.
- (3) Paracrystalline: a third model, made by Kebabinski et al. (1997), is for a 1,000-atom cell containing both CRN-like and paracrystalline Si. The paracrystallites are topologically cubic-Si grains, 1.2–1.6 nm in diameter, with large strains. The unit cell is triclinic, but closely approximates a cube with cell edge length ~ 2.67 nm.

Several variants of these three model types were also examined, but the models described here, with two versions of the CRN, are sufficient to show the essential features that are important to this study.

All diffraction simulations were made assuming kinematical scattering, with the Ewald sphere curvature of a 100 kV electron beam assumed. We did *not* use fast Fourier transform (FFT) methods to compute the diffraction data from a projected potential. Instead, the contribution to the total scattered wave function from each atom was explicitly computed on a 512×512 grid of wavevectors (k_x, k_y), with each pixel representing a $0.05 \times 0.05 \text{ nm}^{-1}$ element of reciprocal space. Patterns therefore spanned a range $-12.8 \leq k_x, k_y \leq +12.7 \text{ nm}^{-1}$. Although avoidance of FFT methods is algorithmically inefficient, it allowed us to maintain high precision on phase changes arising from subtle (i.e., sub-pixel) atomic displacements. All simulations used a Gaussian profile probe size of resolution $R = 1.0$ nm, which is equivalent to a standard deviation in the probe intensity profile of 0.378 nm. This corresponds to a Gaussian profile probe *wave function*, with constant phase in the focal plane, whose standard deviation is a factor $\sqrt{2}$ larger. Diffraction simulations were from isolated unit cells to avoid artifacts related to periodicity. For most simulations, 1,000 random orientations of the cell were selected. The cell origin was also displaced randomly with a standard deviation of $R/2$ to ensure uniform sampling of the model.

Diffuse scattering from large-amplitude atomic displacements was modeled by first selecting a root mean square (r.m.s.) displacement in the range 0.0–0.15 nm. Each atom in the model was randomly displaced from its nominal location along the Cartesian $\pm x, \pm y$, and $\pm z$ axes according to a Gaussian distribution. The displacement distance

distribution is therefore a Maxwellian. For each model orientation, the mean diffraction intensities from 100 randomized disruptions of the model were computed. We did not use the Debye–Waller approximation to emulate the diffuse scattering as this is accurate only for small-amplitude motions—those much smaller than a typical bond distance.

As the r.m.s. displacements of the previous model are too large to be associated with realistic atomic vibrations, we also constructed a simple beam damage model. A predetermined number of atoms were displaced by 1.0 nm in a random direction within the model. Each displacement creates a vacancy at the atom's original location and a one-atom inclusion at the new location. A $\pm \hat{\mathbf{r}}/r^2$ radial strain field was applied to the remaining atoms in the model, centered at each of these sites, r being the radial distance from each site, and $\hat{\mathbf{r}}$ the radial unit vector. The minus sign was used for the vacancy strain, and the plus sign for the inclusion, generating a dipolar strain field. All neighboring atoms within 0.235 nm of the inclusion were pushed away radially to a distance 0.235 nm, and the inverse-square displacement field was applied beyond that radius. To minimize computational costs, the resulting stressed configuration was not relaxed. All atoms in the model end up being disturbed by each beam damage event depending on their distance from the dipole. For each orientation of the model, 100 randomized instances of the displacement field were created, and the individual diffraction pattern intensities added. This was repeated for 1,000 randomized model orientations.

To simulate the situation where beam damage causes different sample regions to tilt relative to each other, frozen phonons were applied to the model. Random sinusoidal displacements were applied to the model along the orthogonal x , y , and z directions. Each diffraction pattern was the incoherent sum of 30 different frozen phonon displacement states, that is, $A_n \sin(k_n x + \phi_n)$ along x , each with random amplitude A_n , phase ϕ_n , and wavevector $k_n = 2\pi/\Lambda_n$, with randomly selected wavelength, Λ_n , between 1 and 6 nm. For each model, a standard deviation amplitude, A , at 2.5 nm wavelength is assigned. The actual phonon amplitude, A_n , is selected randomly from the Gaussian distribution, and then scaled in proportion to the wavelength, so that the effective standard deviation is $\Lambda A/2.5$. This ensures that the amplitude of tilt angle, which is $k_n A_n = 2\pi A/2.5$ (radians), is independent of phonon wavelength. As these are not true dynamical phonons, no attempt was made to quantize the wavelengths with respect to the sample thickness, or to ensure that antinodes occurred at the surfaces. These simulations were applied only to the larger CRN2 model, which was big enough to accommodate one full period of the larger phonon wavelengths.

The effect of electron energy-loss events was simulated by assuming that the phase of part of the primary scattered beam, which has lost a small amount of energy relative to the incident beam energy, has been randomized. Low-energy secondary electrons are ignored. For these simulations, the scattered phases of a predetermined fraction of atoms in

the model were randomized, in the range $0-2\pi$, before computing the intensity. For each model orientation, this was repeated for 100 randomized permutations of random-phase sources, and the mean diffraction pattern intensity returned. This was repeated for 1,000 model orientations.

Spatial incoherence of the illumination was simulated by randomly displacing the probe in the specimen x - y plane, with a Gaussian distribution about the nominal probe location, and computing the diffraction pattern for each location. This was repeated for 30 random displacements for each cell orientation. The mean intensity of this set of 30 patterns then emulates the diffraction pattern for the partially coherent probe. Convolution of the probe and diffracted wave functions does not help us in this instance, as we need the *incoherent* summation of diffraction intensity. In total, 30,000 diffraction computations were made for each model and for each coherence parameter.

The impact of multiple scattering was emulated using a variant of the statistical procedure described in Gibson and Treacy (Treacy & Gibson, 1993; Hÿtch & Stobbs, 1994). Multiple scattering was assumed to be a Poisson-distributed process governed by the parameter t/Λ , where t is the sample thickness and Λ the characteristic thickness at which electrons have been scattered once, on average. The fraction of electrons that are scattered n times, f_n , is assumed to equal the Poisson term

$$f_n = \frac{(t/\Lambda)^n}{n!} \exp(-t/\Lambda). \quad (2)$$

The contribution to the diffracted intensity for those electrons that have been scattered more than once is approximated by a convolution. It is assumed that the first event occurs in the top layer, and the second event in the next layer, and so on. Each layer is expected to have a different structure to the previous. Thus, we first compute and store the full two-dimensional diffraction patterns from 1,000 model orientations and treat these as coming from different layers. We label these I_i , $i = 1-1,000$. For each diffraction pattern I_i , the pattern corrected for multiple scattering, $I_i^{(m)}$, is obtained by convoluting with randomly selected patterns from the set, and summing the contributions, thus

$$I_i^{(m)} = f_0 I_i + f_1 (I_i \otimes \hat{I}_j) + f_2 (I_i \otimes \hat{I}_j \otimes \hat{I}_k) + f_3 (I_i \otimes \hat{I}_j \otimes \hat{I}_k \otimes \hat{I}_l) + \dots \quad (3)$$

The subscripts j , k , and l refer to randomly selected diffraction patterns, from the original set of 1,000, such that $i \neq j \neq k \neq l$. The symbol \hat{I}_k refers to diffraction pattern I_k that has been normalized so that the integrated intensity over the pattern is unity. The symbol \otimes represents a convolution.

Computations were made for $t/\Lambda \leq 2$ and it was sufficient to truncate the convolutions at $n = 4$. FFT methods were used to compute the convolutions of the diffraction patterns. Diffraction pattern arrays were doubled in each dimension to $1,024 \times 1,024$ zero-padded arrays before convolution.

For all computations, the variance and mean intensities were computed as azimuthally accumulated averages.

RESULTS AND DISCUSSION

We start by examining the predictions of the phase-object approximation of kinematical theory for the speckle variance from three models of an amorphous tetrahedral network (Fig. 1a). Two calibrations for the k axis are given, appropriate for amorphous silicon and amorphous carbon, which are the two materials of interest in this study. The kinematical phase-object approximation assumes a single elastic scattering event from *stationary* atoms. We also use fully coherent electron illumination.

The simulated normalized variance for both the random and CRN1 models is constant, with $V(k) \approx 1.0$, when $k > 1.0 \text{ nm}^{-1}$, for both models. No significant variance peaks arise. The variance drops to 0 for $k < 1.0 \text{ nm}^{-1}$ because this region of the diffraction pattern is dominated by the unscattered beam, which is essentially invariant under the weak kinematic scattering approximation. The paracrystalline model gives a normalized variance that exceeds 1.0 for $k > 1.0 \text{ nm}^{-1}$. Broad peaks occur near the crystallographically allowed reflections for cubic-Si, such as 111 (3.19 nm^{-1}), 220 (5.21 nm^{-1}), 311 (6.11 nm^{-1}), 222 (6.38 nm^{-1}), 400 (7.36 nm^{-1}), 422 (9.02 nm^{-1}), etc. (As the C–C bond distances are a factor of 1.6 shorter in diamond than they are in silicon, the peak locations are approximately a factor of 1.6 larger for amorphous carbon—see top axis.) The shoulder on the 111 peak suggests a possible contribution from the nominally forbidden 200 reflection at 3.68 nm^{-1} for Si. The peak broadening arises mainly from the angle subtended by the objective aperture, equivalent to $Q = 1.22 \text{ nm}^{-1}$. The peaks inform us that coherent speckle at these wavevectors is strong because Bragg reflections are switching on and off as different sample regions are probed. In between peaks, the variance background never falls below 1.0.

In principle, the normalized variance could fall below 1.0 if the model is structurally uniform, which would occur if the sample were a perfect single crystal. Then, the intensity variance would be 0, as every sample region would diffract identically. However, a randomly polycrystalline model (not shown) will give a variance that greatly exceeds 1.0 because of the inherent variability in scattering between grains. Although there is a pronounced difference in the normalized variance between the CRN1 and paracrystalline models, the diffraction profiles of these two models are similar (Fig. 1b); both models are essentially “diffraction amorphous.” A model with smaller paracrystallites, 1.0–1.2 nm in diameter for Si (0.65–0.75 nm in diameter for C), has a mean diffraction pattern that resembles the CRN1 remarkably closely (not shown). However, there is a pronounced difference between the random and the CRN1 diffraction profiles.

The observed normalized variance of 1.0 from the random model is expected. The speckle intensity distribution, $P(I)$, from a spatially random distribution of scatterers that are illuminated

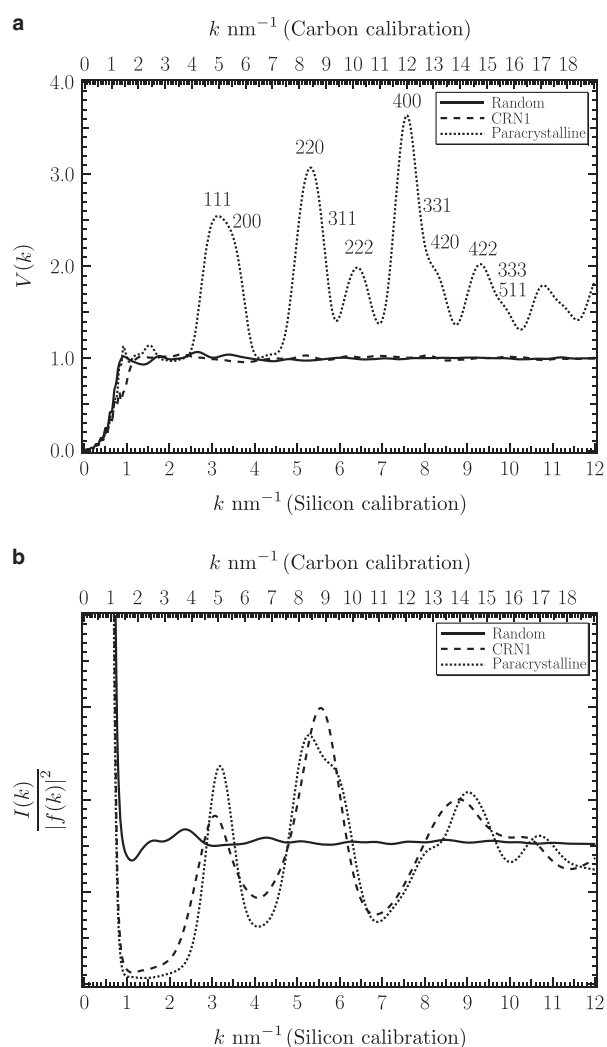


Figure 1. a: Computed normalized speckle intensity variance, $V(k)$, as a function of scattering vector k for three models of amorphous tetrahedral materials. The scaling along k for amorphous Si is provided on the bottom axis of each plot, and for amorphous C at the top axis. The probe size (diffraction-limited resolution) is 1.0 nm. Fully coherent illumination and kinematical scattering conditions are assumed. The random, and continuous random network (CRN1), models give an approximately constant variance of $V(k) \approx 1.0$ for $k > 1.0 \text{ nm}^{-1}$. The paracrystalline model gives a $V(k)$ that exceeds 1.0 everywhere for $k > 1$, and exhibits peaks in the neighborhood of the allowed crystallographic cubic silicon/diamond hkl reflections, which are indicated. The location of the nominally forbidden 200 reflection is also indicated. **b:** Mean diffraction intensity profile, $I(k)/|f(k)|^2$, for a 1.0 nm probe, for the three models. $f(k)$ is the atomic form factor. The intensity scaling is arbitrary. The random model has essentially no peaks. The CRN and paracrystalline models have similar diffraction profiles.

by a spatially coherent source, obeys a negative exponential distribution

$$P(I) = \frac{1}{\langle I \rangle} \exp\left(-\frac{I}{\langle I \rangle}\right), \quad (4)$$

$\langle I \rangle$ is the mean (or, first moment) of the image intensity. This is the intensity distribution expected when the only constraint on the normalized distribution is that the mean

intensity be fixed. Any statistically significant deviation from negative exponential statistics tells us that additional information about the scattering is available. A negative exponential distribution has a second moment given by $\langle I^2 \rangle = \int_0^\infty I^2 P(I) dI = 2\langle I \rangle^2$. The normalized variance is then unity, that is

$$V = \frac{\langle I^2 \rangle - \langle I \rangle^2}{\langle I \rangle^2} = \frac{2\langle I \rangle^2 - \langle I \rangle^2}{\langle I \rangle^2} = 1, \quad (5)$$

as is obtained for the random and CRN models. The normalized variance of a random speckle pattern is independent of scattering vector \mathbf{k} or of probe size R , provided the distribution of scatterers can be regarded as random at the length scale R . This result, valid under the kinematical single-scattering approximation from a random structure with spatially coherent illumination, provides an important starting point for the modeling of speckle from amorphous materials. In models, deviations from this result generally indicate that the structure has nonrandom regions. An information-theoretic justification for the negative exponential distribution is presented in the Full Spatial Coherence: Negative Exponential Speckle Statistics section of the Appendix.

Not all researchers in FEM obtain this underlying normalized variance of 1 in their variance-simulation codes. The approximation used by Stratton & Voyles (2008) and Li et al. (2013) is inherently kinematical, but their model introduces incoherence between scattering regions resulting in a background variance that falls below unity. Bogle et al. (2007) introduced incoherence into their simulations by breaking up their model into layers and combining intensities.

Experimental results, however, do not reproduce our simulations. Figure 2 shows a tilted dark-field image of a ~ 30 nm thick amorphous sputtered carbon film, aC1. The image was taken with 200 kV electrons, and a resolution of

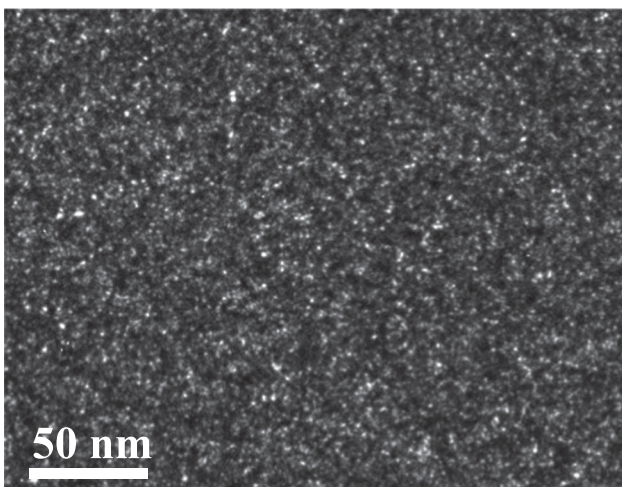


Figure 2. Tilted dark-field image of a ~ 30 -nm thick sputtered carbon film (aC1), taken with 200 kV electrons at an illumination tilt of $q = 5.3 \text{ nm}^{-1}$. The image resolution is $R \approx 1.0$ nm. Images at other q values are qualitatively similar, although the speckle contrast varies, and the exposure time increases with q in order to keep the mean intensity constant.

1.0 nm, with an illumination tilt centered at $k \approx 5.3 \text{ nm}^{-1}$, corresponding to the first peak in the normalized variance for carbon in Figure 1a. Bright and dark speckles are visible, appearing to be distributed randomly, with the smallest speckle diameters measuring about 1.0 nm in width, consistent with the instrumental resolution. This image is part of a series of tilted dark-field images spanning illumination tilts over the range $2\text{--}10 \text{ nm}^{-1}$. The normalized variance, $V(q)$, of this set of images is plotted in Figure 3. The experimental $V(q)$ is not constant and has broad peaks, indicating that the structure is not entirely random and that some form of MRO is present. Further, the normalized variance is low everywhere, averaging 0.037. It is 0.026 in the dips, which is a factor of about 40 lower than kinematical theory predicts for a random structure.

One possibility is that spatial incoherence in the illumination is suppressing speckle variance. Spatial incoherence can be thought of as arising from multiple, mutually incoherent, sources in the illumination that give an angular spread in illumination direction. If there are $m \geq 1$ such sources (m does not need to be an integer), with $m = 1$ corresponding to fully spatially coherent illumination, the intensity distribution is no longer a negative exponential, but follows a Gamma distribution (Dainty, 1975; Goodman, 1975a, 1975b):

$$P(I) = \frac{m^m}{\Gamma(m)} \frac{I^{m-1}}{\langle I \rangle^m} \exp\left(-\frac{mI}{\langle I \rangle}\right). \quad (6)$$

$m = 1$ recovers the negative exponential statistics of equation (4)—the Gamma function is such that $\Gamma(1) = 1$. The normalized variance of the Gamma distribution is $V = 1/m$. An information-theoretic justification for the Gamma distribution statistics is given in the Partial Spatial Coherence: Gamma Distribution Speckle Statistics section of the Appendix.

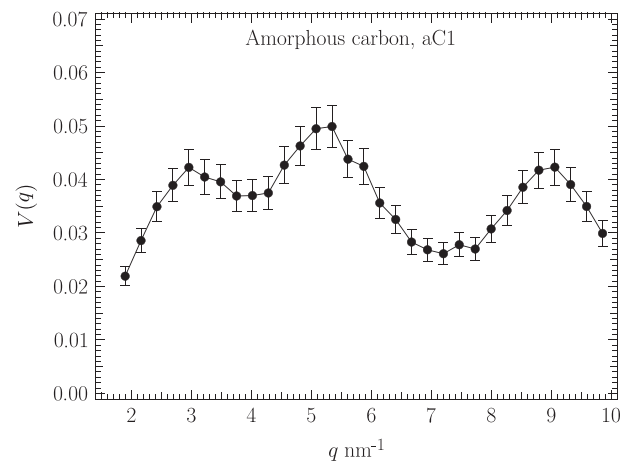


Figure 3. Normalized variance $V(q)$ from a ~ 30 -nm thick sputtered amorphous carbon film (aC1) obtained under tilted dark-field fluctuation electron microscopy conditions at 200 kV. The resolution is $R \approx 1.0$ nm. The normalized variance was obtained by analyzing the intensities in tilted dark-field images, such as that shown in Figure 2. q is the illumination tilt vector amplitude, which is equivalent to the scattering vector amplitude k . The error bars are set at $\pm 8\%$ and represent typical experimental variations.

To explain the plot in Figure 3, we need an illumination incoherence equivalent to $m \approx 40$. Although the spatial coherence was not measured in this experiment, it is known that the illumination conditions that were used were capable of producing high-resolution bright-field images, suggesting that $m \leq 3$, and certainly not 40.

The intensity histograms of all of the amorphous carbon-tilted dark-field images contributing to the normalized variance plots in Figure 3 were fitted against a Gamma distribution, with the mean intensity, $\langle I \rangle$, and the incoherence parameter m as adjustable factors. All of the intensity distributions fit a Gamma distribution well, two of which are presented in Figure 4. None of the tilted dark-field images showed negative exponential statistics. All of the fitted m values exceed 26. The best fits occur for those images taken at k values in the variance dips in Figure 3. This is presumably because the speckle at the peaks contains additional

structural information. The Gamma distribution assumes that the only information available about the experiment is the mean intensity, $\langle I \rangle$, and the m parameter (Partial Spatial Coherence: Gamma Distribution Speckle Statistics section of Appendix). In the experiments, the image mean intensity was held approximately constant for all micrographs, $\langle I \rangle \approx 100$. The effective m value, which also controls the spread of the distribution, varies between about 42 in the dips (narrower intensity spread) to about 26 at the peaks (broader spread). Exposure times needed to be increased as q increased, to offset the decrease in atomic-scattering factor at increasing q , and m tended to be high at these higher q values where there are no pronounced peaks. In summary, the effective incoherence parameter, m , varies across the normalized variance plot, decreasing at the peaks and increasing in the dips and at high q . This observation is inconsistent with the conjecture that illumination incoherence alone controls m , which should have been constant for the whole $V(q)$ plot.

The fitted m parameter at each of the points, q , does not generally equal $1/V(q)$. This would be true only if the speckle statistics fit the Gamma distribution exactly. For example, the variance peaks for the paracrystalline model in Figure 1 would imply m values less than 1, which cannot be related in any simple way to incoherence. The variance peaks are present in that plot because the underlying structure is not random. Although the fitted value of m varies across the variance plot, it is reasonable to presume that this variability is associated with structural order within the sample with an underlying constant incoherence contribution arising from the experimental conditions.

In a correlograph and FEM study of amorphous Si using STFEM (Gibson et al., 2010), normalized variance plots gave values of $1/V \approx 100$ in the dips. This is despite the fact that the illumination was known to be highly spatially coherent, as determined by comparing the probe intensity profile with that expected from the Airy intensity function from a circular aperture. It is clear that spatial coherence alone cannot be responsible for the suppression of speckle variance.

The evidence suggests that the electron-scattering processes within the sample introduce a *decoherence* that mimics some of the effects of illumination spatial incoherence—at least to the extent of reproducing the Gamma distribution statistics—with an associated m decoherence parameter.

Illumination spatial coherence is known to be an important parameter for suppressing speckle contrast. Figure 5 shows experimental data at 200 kV from the amorphous silicon sample, aSi, showing the effect of spatial incoherence on the normalized variance. All plots were obtained with a nominal, diffraction-limited, probe resolution of 2.4 nm. The JEOL preset spot sizes of 0.5 (high spatial coherence) and 2.4 (low spatial coherence) were used. The experimental full-width half-maxima for these spot sizes were measured at 2.3 and 3.0 nm, respectively. Results for two different exposure times are shown for each. The smaller spot size generates a lower beam fluence rate, rendering data

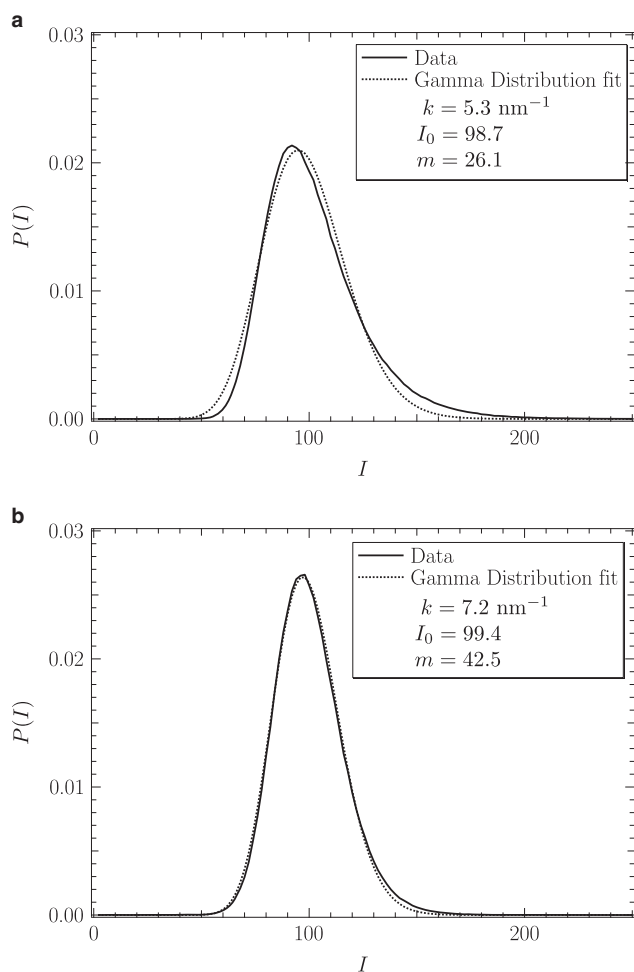


Figure 4. Intensity distribution histograms, $P(I)$, for two of the tilted dark-field images of amorphous carbon, aC1, that form the normalized variance plot in Figure 3. **a:** Illumination tilt $q = 5.3 \text{ nm}^{-1}$, where there is a peak in the normalized variance. This is the intensity histogram of Figure 2. **b:** Illumination tilt $q = 7.2 \text{ nm}^{-1}$, where there is a dip in the normalized variance. The plot from the variance dip, (b), provides a better fit to a Gamma distribution than does the plot from the variance peak, (a).

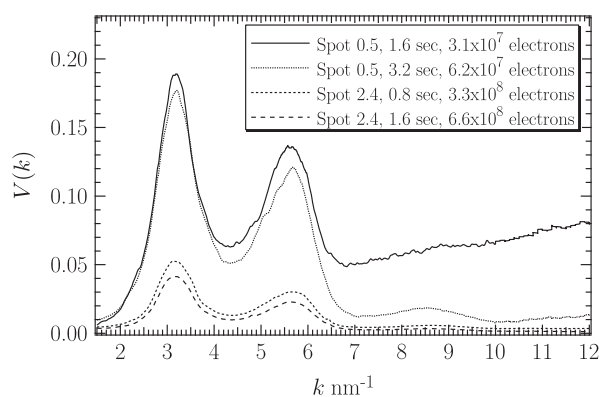


Figure 5. Experimental data from amorphous silicon, aSi, showing the effect of spatial incoherence on the normalized variance. All plots were obtained with a nominal, diffraction-limited, probe resolution of 2.4 nm at 200 kV. The JEOL preset spot sizes of 0.5 (high spatial coherence) and 2.4 (low spatial coherence) were used. The experimental full-width half-maxima for these spot sizes were measured at 2.3 and 3.0 nm, respectively. The exposure conditions are given in the legend.

more prone to noise, unless longer exposure times are used. Higher fluence results in lower variance. The plots for spot size 0.5 are for essentially fully spatially coherent illumination. An image of the focused probe intensity follows closely the idealized Airy intensity profile, with an amplitude of 0.016 at the first “zero” relative to the central intensity. For spot size 0.5 at 0.8 s exposure time, $1/\langle I(k) \rangle$ shot noise dominates the normalized variance at high k , causing $V(k)$ to rise with increasing k . The peak variance is $V \approx 0.19$ at $k \approx 3.1 \text{ nm}^{-1}$. The variance in the dip near 4.4 nm^{-1} is about 0.07. Both the first peak and the following dip are about a factor of ~ 15 less than the kinematical calculation in Figure 1a.

Recently, Li et al. (2014) also pointed out that normalized variance is suppressed by this form of spatial incoherence. As stated in the introduction, spatial coherence is a useful controllable parameter in FEM.

The impact of electron beam energy on the measured variance was explored by comparing the variance of amorphous carbon (Fig. 6a) with amorphous sputtered silicon (Fig. 6b) at 80 and 200 kV. These FEM data were collected in STFEM mode with a 1.3 and 1.5 nm resolution probe, respectively. There is significant spatial incoherence in the illumination in these experiments, but it is held approximately the same at each voltage for each sample. The background variance is less than 10^{-3} , suggesting $m \approx 1,000$ —a suppression of three orders of magnitude. The fluence at each voltage was held approximately the same; $3.6 \pm 0.6 \times 10^9$ electrons/nm² for both the amorphous carbon and amorphous silicon. The fluence is high in these experiments in order to suppress the $\sim 1/\langle I(k) \rangle$ shot noise that would otherwise dominate the normalized variance at high- k values. The high fluence rate (beam current) is achieved at the expense of spatial coherence. As we saw in Figure 5, high illumination spatial coherence increases the variance of the

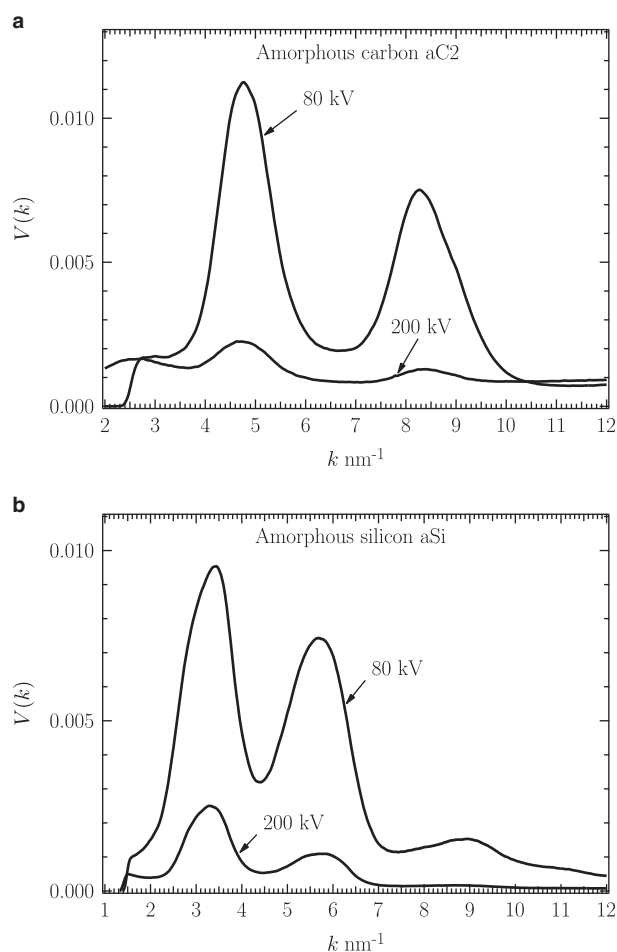


Figure 6. Normalized variance plots obtained by STFEM for 80 and 200 kV electrons for; (a) the amorphous carbon film, aC2; (b) the amorphous silicon film, aSi. The spatial coherence and the fluence are approximately the same at each voltage. The normalized variance at 200 kV in each sample is strongly suppressed relative to that at 80 kV. Peaks at high k in the 200 kV amorphous Si data are proportionally more suppressed than those at 80 kV.

first amorphous Si peak, at $\sim 3.1 \text{ nm}^{-1}$, 200 kV by a factor of ~ 80 . This still leaves an anomalous speckle suppression factor of 10–20 in the variance background.

Both materials exhibit similar variance plots, with two pronounced peaks and a weaker third peak at higher k , because they are both tetrahedral materials based on the cubic diamond structure. The different peak locations along k is because of the difference in the C–C and Si–Si bond distances (~ 0.15 and ~ 0.24 nm, respectively). For each material, higher voltage reduces the measured normalized variance, despite the fact that the illumination spatial coherence is unchanged. By kinematical scattering theory, there should be little difference in normalized variance as a function of voltage. For both materials, the variance peaks at 200 kV are increasingly suppressed as k increases relative to the peaks at 80 kV. The peak at $k \approx 9.0 \text{ nm}^{-1}$ in the plots for amorphous Si (Fig. 6b) has almost vanished in the 200 kV data.

It is a characteristic of all FEM normalized variance plots that peaks in $V(k)$ fade strongly as k increases, even though kinematical simulations show persistent peaks at much large k values (Treacy & Gibson, 2012). This effect can be seen by comparing the computed paracrystalline silicon variance plot in Figure 1 with the data in Figure 6. Introduction of a physically reasonable Debye–Waller temperature factor, with r.m.s. vibration amplitude less than 0.01 nm, does not account for the high- k suppression of variance.

Normalized variance can also decrease with increasing exposure time in STFEM experiments. Figure 7 shows the normalized variance, obtained with a probe of resolution $R \approx 2.0$ nm, for a sample of UNCD where the crystalline grains are typically ~ 2 –10 nm in diameter. Strong peaks appear at the cubic diamond reflections, which are indicated on the plot. The strongest variance peaks occur for the shortest exposure time for individual diffraction patterns, 0.01 s. As the exposure time is increased to 0.1 s, the overall height of the normalized variance plot is approximately halved in the two main peaks.

When the probe is kept stationary on the sample, diffraction patterns are observed to twinkle. Strong speckle appears and disappears at time scales of the order of 1 s. This effect is most pronounced at higher voltages. At short time scales, down to 0.01 s, shot noise dominates the twinkling, which is pronounced. Figures 8a and 8b compare two diffraction patterns from amorphous silicon obtained with a probe of resolution 2.4 nm ($Q = 0.5 \text{ nm}^{-1}$) using 200 kV electrons. The exposure time for consecutive patterns is 3.2 s. Figure 8c shows the intensity difference between the two patterns, pattern (a) minus pattern (b). A bright region in (c) indicates that a bright speckle occurs in (a) but is missing in (b), and dark means that a new bright speckle appeared in (b). Gray indicates that the intensity is relatively unchanged.

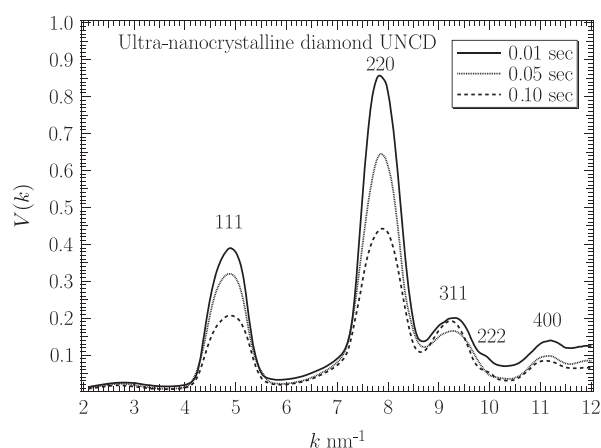


Figure 7. Experimental STFEM normalized variance plots for a thin sample of nanocrystalline diamond with grains ranging 2–10 nm in diameter. Strong variance peaks arise at the cubic diamond main reflections, 111, 220, 311, etc. Because of these strong coherent Bragg reflection peaks, plots with short exposure times are not dominated by shot noise. The variance at all k values decreases as exposure time (fluence) increases.

The twinkling indicates that electron beam interactions with the amorphous sample are modifying, or damaging, the structure at slow (i.e., at human-observable) time scales (10 ms and up). The integrated effect over the exposure times needed to acquire low noise data lowers the speckle contrast, thereby lowering the measured speckle variance.

In Figure 9, we present computational results for the same three models of amorphous silicon that were presented earlier in Figure 1; a CRN model (CRN1), a random model, and a paracrystalline model. In these simulations atoms were randomly displaced about their mean positions, with a Maxwellian probability profile, and diffraction patterns were averaged over many such random displacements. Such motions, integrated over the data acquisition time, generate a diffuse scattering background that suppresses intensity contrast. For the CRN1 model (Fig. 9a) displacements comparable with normal phonon r.m.s. vibration amplitudes, 0.005 nm, have only a small effect on the variance, but suppressing the variance increasingly at higher scattering vector, k , as expected. Larger r.m.s. displacements suppress variance strongly, particularly at high k , as is observed experimentally. For an r.m.s. displacement of $\nu = 0.15$ nm, which is more than half of a Si–Si bond distance, variance is suppressed by a factor of about 5 at the peaks, and by about 20 at the dips.

The variance profile at high r.m.s. displacements in the CRN1 model resembles strongly the experimental data obtained for amorphous silicon (compare with Fig. 6b), although the computed variance is still too high by almost an order of magnitude.

Curiously, the peaks do not appear in the static ($\nu = 0.0$ nm r.m.s. displacement) model, where the normalized variance is approximately constant and equal to 1.0, as expected for a random model. The emergence of peaks, in the experimentally observed locations as r.m.s. displacement increases, is not a computational artifact. The same peaks emerge for several other CRN models available to the authors. The variance plots for the random model (Fig. 9b) show no significant peaks. In that case the variance decays, essentially monotonically, with increasing k .

The paracrystalline model (Fig. 9c) already has strong peaks even without any r.m.s. displacement, as pointed out earlier. As the r.m.s. displacement amplitude increases, the variance is suppressed, particularly at high k , leaving behind essentially the same peaks that appear in the CRN model. The main differences are that the paracrystalline peaks have a higher variance and are narrower.

The r.m.s. displacements needed to reproduce the experimental variance data are far too large to be associated with uncorrelated Einstein-type vibration modes. We explored the possibility that the large apparent vibration amplitudes may arise from flexural, or tilting, motions of different sample regions relative to each other while under the beam. To emulate this in a computationally simple way, we applied large-amplitude frozen phonon displacements along the x , y , and z directions. The computational details are provided in Computational Details section. The results are shown in Figure 10. For r.m.s. tilt angles of 50 mrad and

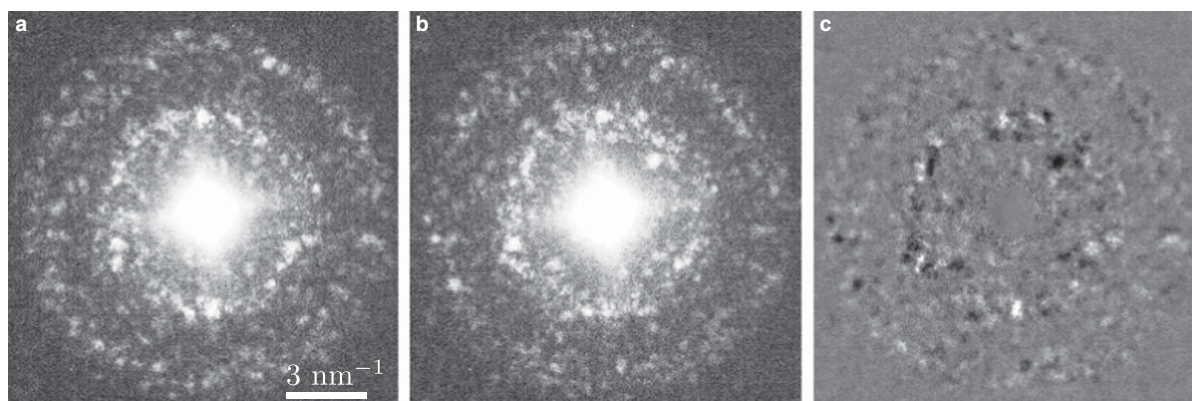


Figure 8. a,b: Consecutive microdiffraction patterns taken from the same region on the amorphous Si sample, aSi, using 200 kV electrons and probe-forming aperture $Q = 0.5 \text{ nm}^{-1}$. Exposure time for each was 3.2 s. **c:** The difference pattern, (a) minus (b), showing that the speckle pattern is not constant with time. Bright regions in (c) show that pattern (a) has more intensity, dark regions show that (a) has less. Gray means no significant difference.

above, the characteristic a-Si variance peaks near 3.1 , 5.9 , and 8.9 nm^{-1} appear. However, the value of the variance itself is not strongly suppressed, and for large tilts, it rises at small k .

Another approach to modeling the effects of local tilts would be to subdivide the model into smaller grains, randomly tilt them through small angles, and compute for (say) 100 randomized instances, but that was not pursued in this study. A related computation was done by Bogle et al. (2007) who used 200 incoherent layers. However, their tilts were structurally uncorrelated.

We investigated a simple model of beam damage, where a predetermined number of Si atoms are displaced by 1.0 nm in a random direction within the model. Each displacement creates a vacancy at the atom's original location and a one-atom inclusion at the atom's new location. A simple strain field emanating from each inclusion and vacancy is applied to the whole model. Details are provided in Computational Details section. Figure 11 shows how the normalized variance is affected when 0–200 damage events occur in the 4,096-atom CRN1 model. The most pronounced effect in this model is that the variance at high k is suppressed as the damage density increases. Weak peaks near the crystallographic cubic-Si 111 and 220 reflections appear but do not match the experimental profile. Although the model is undoubtedly oversimplified, it does show variance suppression and the appearance of experimentally observed peaks in the CRN model.

Most FEM experiments are conducted on samples that are in the neighborhood of 10 – 40 nm thickness. Our Si and amorphous carbon samples were about 20 – 30 nm thick and our nanocrystalline diamond samples are nearer 50 – 60 nm in thickness. At these thicknesses multiple scattering is expected to be significant. Multiple scattering on its own should not introduce incoherence. For example, dynamical scattering is a fully coherent process; phase relationships between scattered waves are preserved even though the scattering is convoluted (Hirsch et al., 1977). However, in the presence of displacement decoherence, where the phase relationship between scattered beams is already

compromised, multiple scattering is expected to smooth out speckle further.

We modeled multiple scattering as an incoherent convolution of individual diffraction patterns; that is, a convolution of diffraction intensities as opposed to diffraction wave functions. This is equivalent to imposing incoherence between the diffraction patterns of successive layers. Multiple scattering events are assumed to follow Poisson statistics, as elaborated in Computational Details section. Although not a formally accurate approach to multiple scattering, our procedure should give a reasonable idea of the impact of multiple scattering on speckle statistics. Figure 12 confirms that multiple scattering does suppress speckle variance for the CRN1, random, and paracrystalline models. A thickness of $t/\Lambda = 2$ suppresses variance by about an order of magnitude. Variance is suppressed slightly more at high k , but not by enough to explain experimental observations.

Weak variance peaks at the cubic-Si 111 and 220 positions become more pronounced in the CRN1 model at around $t/\Lambda \approx 1$. These peaks do not appear in the random model. It appears that multiple scattering may also suppress noisy speckle (arising from random constructive/destructive interference) more than it does structurally correlated speckle from MRO. This is supported by the presence of strong peaks in the paracrystalline model (Fig. 12c). Although the peaks themselves are suppressed by the multiple scattering, the dips between the peaks (arising from random structural correlations) are suppressed even more, and so the peak contrast persists at high k .

Appropriate values of Λ for carbon and silicon are not known accurately. They are clearly governed by both the elastic scattering cross-sections, which are fully coherent, and the inelastic scattering cross-sections, which are incoherent. We expect Λ to be comparable with typical extinction distances for elastic scattering, in the range 10 – 30 nm for silicon with 200 kV electrons.

A simple model was tested for energy-loss events, where the phase of the scattered wave from each atom that

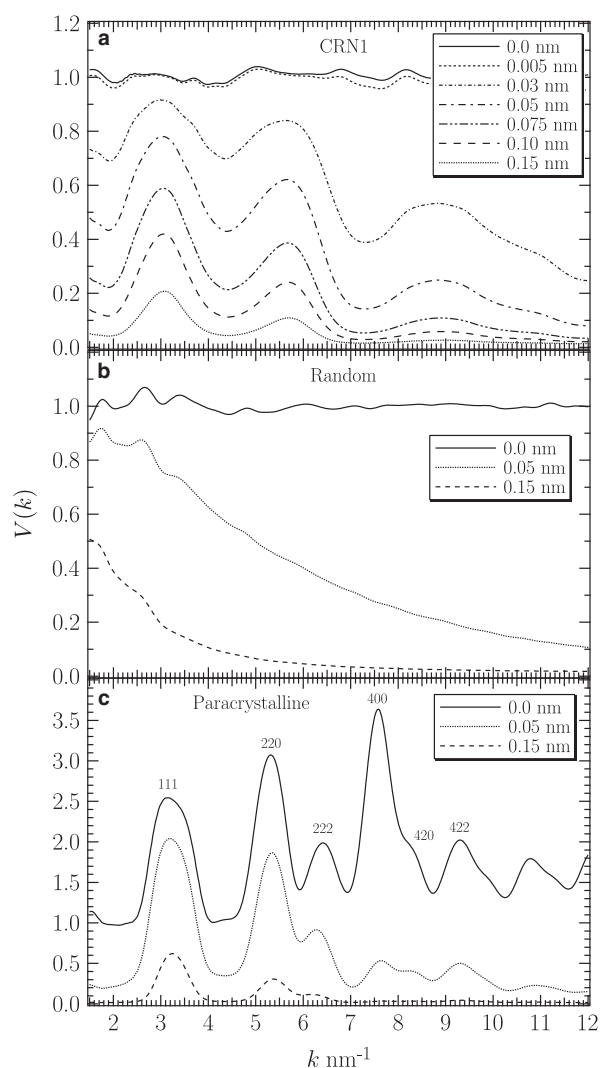


Figure 9. Computed variance plots for three models of amorphous silicon, assuming randomized and uncorrelated atomic displacements that are induced by interactions with the electron beam. Displacement root mean square (r.m.s.) amplitudes, ν , between 0.0 and 0.15 nm are presented. **a:** Continuous random network (CRN1) model. **b:** Random model. **c:** Paracrystalline model. These are the same models that were used in Figure 1. Variance is strongly suppressed with increasing r.m.s. displacement amplitude. Peaks emerge in the CRN1 model that match qualitatively the experimental data. These peaks are broadened versions of the peaks obtained for the paracrystalline model, but with lower peak height. The random model has no significant peaks.

experiences an energy-loss event is randomized. This model considers only the high-energy beam, ignoring secondary electrons, and assumes that exposure times are short enough that the contribution from each atom is either entirely coherent or entirely random. Randomization has essentially no effect on the CRN1 (Fig. 13a) and random models (not shown), where the variance from a random scatterer remains equal to 1. For the paracrystalline model, phase randomization suppresses the variance peaks such that when most of

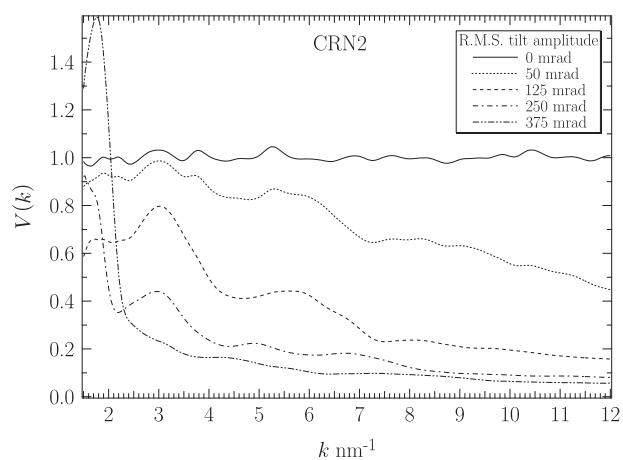


Figure 10. Normalized variance plots for amorphous continuous random network (CRN) silicon, computed for a frozen phonon model. Standard deviations on local tilt range between 0 and 375 mrad. The 100,000-atom CRN model CRN2, 12.4 nm thick, was used to accommodate the long-wavelength phonons. Peaks appear at the experimentally observed locations.

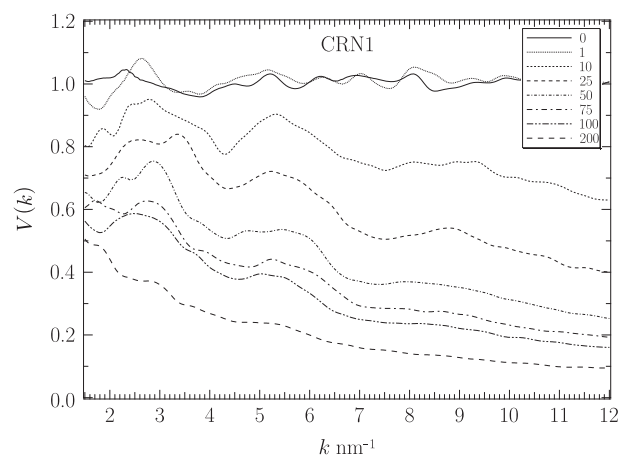


Figure 11. Variance plots for the 4,096-atom continuous random network (CRN1) silicon model, for a simplified beam damage model where a dipolar vacancy–interstitial strain field arises when an atom is displaced. The total number of atoms displaced ranges from 0 to 200 (less than 5% of the total), and are indicated in the plot legend. For light damage (10–100 displacements), peaks emerge that correspond approximately to the experimental peaks.

the scattering is randomized (i.e., more than 85%, Fig. 13b) the variance resembles that from the CRN model, $V(k) \approx 1$ for all k . Phase randomization suppresses the coherent-structure peaks, but not the random-structure background. This is the expected result from a phase-randomized wave function (Treacy & Gibson, 2012).

The impact of illumination spatial incoherence was computed. This was modeled as random, Gaussian-distributed, displacements of the probe about the nominal position. This is equivalent to considering a source with a Gaussian solid angle profile with respect to the focal plane at the specimen, from which electrons are being randomly

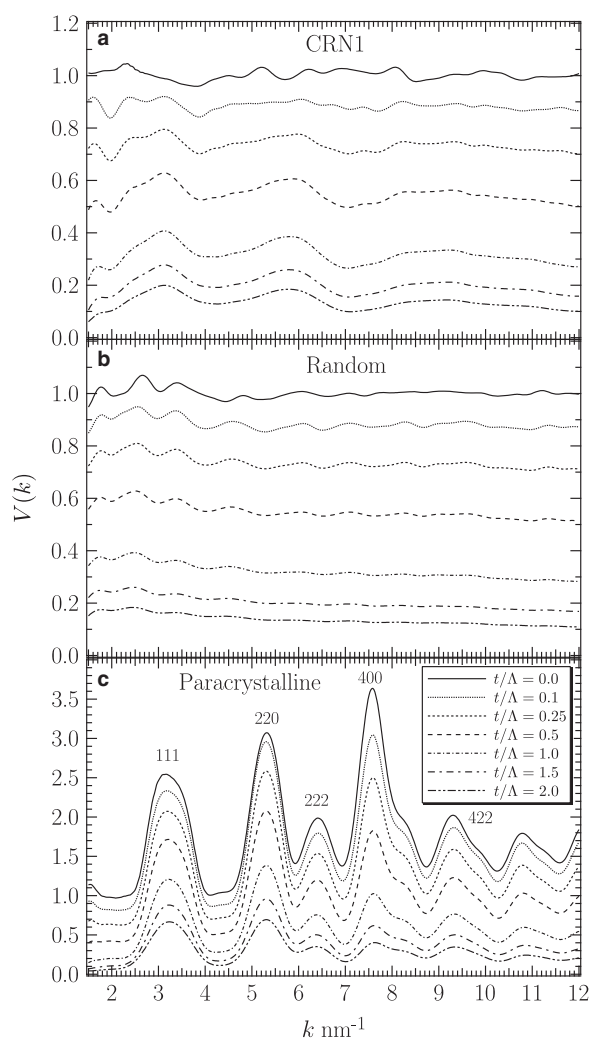


Figure 12. The role of multiple scattering on the computed normalized variance plots for amorphous silicon. The multiplicity of scattering is assumed to be controlled by Poisson statistics, which are governed by the ratio of the sample thickness, t , to some characteristic scattering length, Λ . Seven values for the ratio t/Λ are modeled in the range $0 \leq t/\Lambda \leq 2$. **a:** continuous random network (CRN1) model. **b:** Random model. **c:** Paracrystalline model. These are the same models that were used in Figures 1 and 9. For all models, variance is suppressed by a factor of about 2 when $t/\Lambda = 0.5$, and a factor of about 3 when $t/\Lambda = 1.0$. In the CRN1 model, weak peaks at the experimentally observed positions emerge.

emitted (i.e., they are mutually incoherent). The computational details are described in Computational Details section. Spatial incoherence suppresses variance, as expected. The 2 nm r.m.s. displacement suppresses variance by a factor of $m \sim 5$ when the probe resolution is 1 nm. However, the high- k peaks are not strongly suppressed in the paracrystalline model (Fig. 14c).

The results of these various models are summarized in Table 1.

It is likely that all of these processes, beam damage, multiple scattering, energy loss, and illumination incoherence occur concurrently in our experiments. Figure 15 shows one

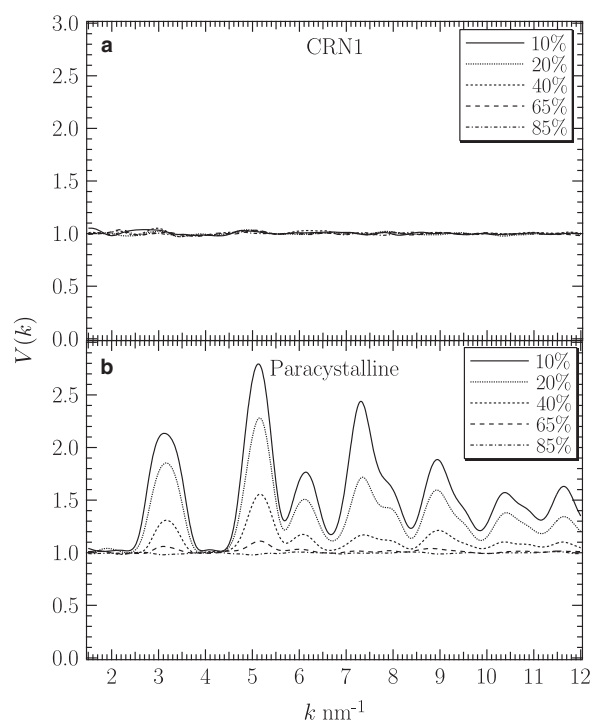


Figure 13. Simulations of the effect on normalized variance from phase randomizations after scattering with energy loss. **a:** continuous random network (CRN1) model. **b:** Paracrystalline model. The legend indicates the percentage of atoms in the model whose scattered phase has been randomized. Phase randomization does not affect the normalized variance of the CRN1 model, which remains close to unity for all k . The peaks rising above unity in the paracrystalline model (coming from structural correlations) are suppressed by the random phase, giving a normalized variance near unity. Background variance is not suppressed by phase randomization, staying near $V(k) \approx 1$.

outcome for the CRN1 model where it is assumed that the r. m.s. damage displacement has a less ambitious value of $\nu = 0.05$ nm, and that multiple scattering corresponding to $t/\Lambda = 1$ is occurring. Plots for various levels of probe incoherence are shown, for probe instability standard deviations, σ , of $0.1 \text{ nm} \leq \sigma \leq 2.0 \text{ nm}$. The probe width (resolution) is set at $R = 1.0$ nm. When $\sigma = R$ variance is suppressed by a factor of 2, and when $\sigma = 2R$, it is a factor of about 4. Many different combinations of parameters are possible, but were not explored because of the long computation times needed. Importantly, the experimentally-observed peaks emerge from the CRN model, as well as from the paracrystalline model. Moreover, importantly, significant variance suppression occurs at high k .

In experimentally constrained structural relaxation experiments, both diffraction and variance data are used in a simulated annealing program to obtain a generic structure that is consistent with the data (Biswas et al., 2005; Hwang et al., 2009; Borisenko et al., 2012). The variance discrepancy in those studies was dealt with by imposing a simple multiplicative factor, corresponding to a nominal m that is the same across the whole $V(k)$ pattern. Typical values are

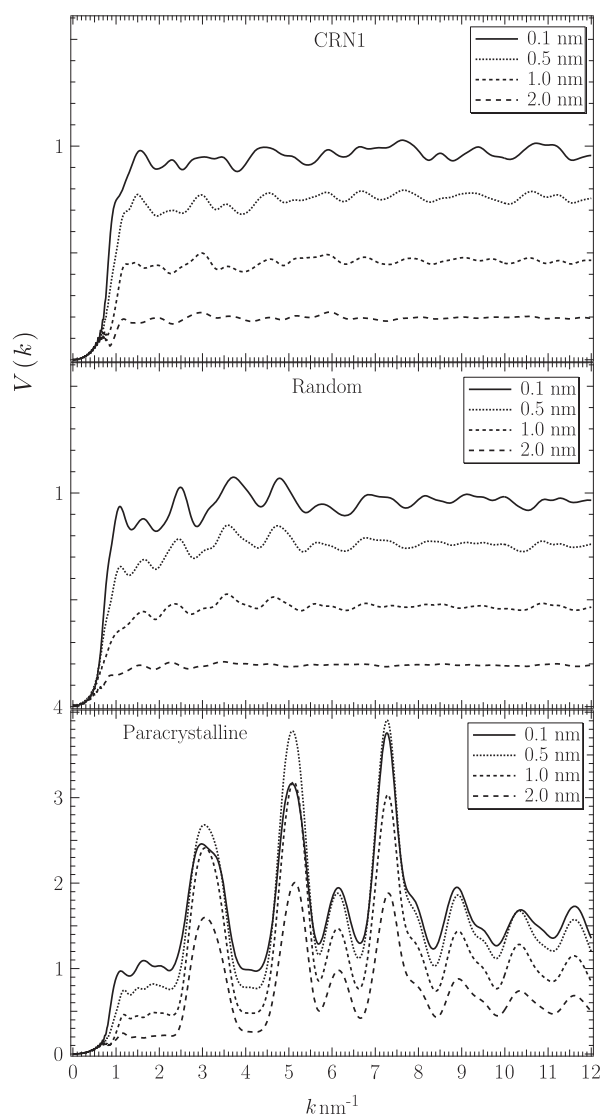


Figure 14. Simulations of the effect of spatial incoherence on the normalized variance. The incoherence was modeled as random, Gaussian-distributed, movements of the probe about the nominal location. The probe resolution was 1.0 nm, and root mean square probe displacements of 0.0, 0.5, 1.0, and 2.0 nm are shown. **a:** continuous random network (CRN1) model. **b:** Random model. **c:** Paracrystalline model. Spatial incoherence suppresses variance, but does not preferentially suppress variance at high k . The small peaks in the CRN1 and random models are from the low sampling statistics in these simulations and are not structurally significant.

$10 \leq m \leq 100$, with the low m values tending to arise in DFFEM mode, and the high m values in STFEM mode. Our results make it clear that the variance suppression is not uniform across the $V(k)$ plot, and that it varies depending on whether it is part of the variance background or a peak in the plot.

We explored this dependence for the Einstein-vibration displacement decoherence model. Figure 16 shows the dependence of the fitted normalized variance peak areas (on a logarithmic scale) for the paracrystalline model shown in Figure 9c, as a function of atomic r.m.s. displacement amplitude ν . The variance plots of Figure 9c, where plots for

Table 1. Summary of Simulation Results.

Simulation	Summary of Variance Output
Simple kinematical with static atoms and no energy loss or multiple scattering	Strong variance peaks in paracrystalline models that persist at high k . No peaks from the CRN model. Background variance is 1.0 for scattering out of the probe (dark-field conditions) (see Fig. 1a)
Random atom displacements averaged over time	Variance peaks in paracrystalline models are suppressed, most strongly at high k . In the CRN, pronounced peaks emerge at low k at the experimentally observed positions. No peaks appear in the random model. Background variance falls significantly below 1.0 in all models (see Fig. 9)
Frozen phonons averaged over time	Variance is suppressed. Peaks appear in the CRN at the experimentally observed positions. Variance at high k is strongly suppressed (see Fig. 10)
Damage with strain, accumulating over time	Results are similar to the frozen phonon model. Peaks appear in the CRN model (see Fig. 11)
Energy loss. Phase randomization of a fraction of the scatterers, averaged over time	Variance peaks are suppressed. Background variance remains at 1.0 (see Fig. 13)
Spatial Incoherence. Probe is displaced randomly over time	Variance is uniformly suppressed. Peaks at high k remain visible. No peaks appear in the CRN or random models (see Fig. 14)
Multiple scattering. Modeled as an incoherent, Poisson-distributed process	Variance is uniformly suppressed. Peaks at high k remain visible. Weak peaks appear in the CRN model at the experimentally observed locations. No peaks appear in the random model (see Fig. 12)

CRN, continuous random network.

three values of ν are shown, were fitted to a set of Gaussian peaks and a constant background. The various peaks and background have different dependencies on k . The 111 and 220 normalized variance peak areas increase initially as displacement amplitude ν is increased. The 400 peak area falls rapidly. This behavior can be understood by examining the form of the structure factor for these reflections from a single crystal. All atomic displacements decrease the 400 structure factor by taking it off-resonance. However, small displacements do not adversely affect the 111 structure factor as it is not a fully resonant reflection with every atom scattering in phase. It is clear that a simple multiplicative factor can not capture all of the subtlety of the variance suppression when there is strong MRO present.

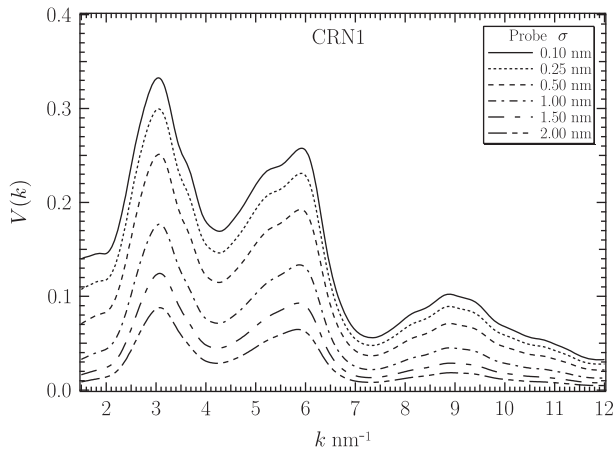


Figure 15. Simulation of the combined effect of atomic displacements, multiple scattering and illumination spatial incoherence for the continuous random network (CRN1) model. The root mean square damage displacement is set at $\nu = 0.05$ nm and $t/\Lambda = 1$ for multiple scattering. Plots are for probe instability standard deviations, σ , in the range $0.1 \text{ nm} \leq \sigma \leq 2.0 \text{ nm}$. The probe width (resolution) is set at $R = 1.0$ nm. When $\sigma = R$, variance is suppressed by an additional factor of about 2, and when $\sigma = 2R$, it is a factor of about 4.

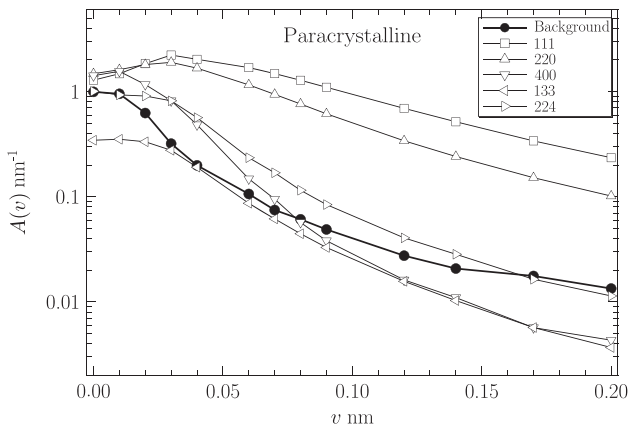


Figure 16. Plot showing the calculated normalized variance peak areas, $A(\nu)$, on a logarithmic scale, as a function of root mean square displacement amplitude, ν , for the paracrystalline model. The calculated $V(k)$ plots of Figure 9c, where plots for three vibration amplitudes are presented, were fitted to a series of Gaussian peaks with a constant background. The fitted variance background (the area under a 1 nm^{-1} reciprocal-width window in k) is also plotted (filled circles). In the legend, each trace is labeled according to a cubic silicon reflection associated with the peak. Peak areas and background do not fade away at the same rate as a function of ν . In some instances, normalized variance peak areas increase as ν increases when $\nu < 0.04 \text{ nm}^{-1}$. In experiments, it is the 111, 220, and 224 peaks that persist, which are the three peaks that fade the slowest in these simulations.

DISCUSSION

Our results indicate that FEM variance is strongly suppressed by structural disruptions caused by the electron

beam. A simple model indicates that large Einstein-type, uncorrelated atomic vibrations as large as 0.15 nm can reproduce the experimental data. This is large compared with the bond distances, and the model is clearly too simple. Multiple scattering, in the presence of randomized atomic displacements, can play an important role in variance suppression in thicker samples.

When an electron is scattered through k by an atom, the deflection imparts a momentum hk , where h is Planck's constant. The atom, of mass $M(Z)$ recoils with an equal and opposite momentum, where Z is the atomic number. The energy associated with the atom's recoil is $h^2k^2/2M(Z)$. The importance of this energy can be evaluated by comparing it with $k_B T$, where k_B is the Boltzmann's constant and T the specimen temperature. If the recoil energy is comparable with $k_B T$ then we expect the typical displacement amplitude from the recoil to be equivalent to the thermal displacement amplitude. For a differential scattering cross-section $\sigma(k, Z)$, the mean recoil energy, relative to $k_B T$, is given by

$$\langle E/k_B T \rangle = \frac{h^2 \langle k^2(Z) \rangle}{2M(Z)k_B T} = \frac{h^2 N_A}{2k_B T A(Z)} \frac{\int_0^\infty k^3 \sigma(k, Z) dk}{\int_0^\infty k \sigma(k, Z) dk}, \quad (7)$$

where $A(Z)$ is the atomic mass (in kg units) and N_A the Avogadro's number.

For $Z > 2$, this ratio is less than 0.6 for all the elements. It is 0.48 for carbon and 0.27 for silicon. Clearly, most scattering events disturb the atoms much less than the room temperature vibration amplitude.

The differential scattering cross-section for neutral atoms can be modeled fairly well as a Gaussian curve, $a \exp(-bk^2)$. The Doyle–Turner parameterization uses four such Gaussians plus a constant offset to emulate the persistent tail at high k (Doyle & Turner, 1968). The Kirkland parameterization uses four Gaussians and four Lorentzians, the latter to emulate the high- k tail (Kirkland, 1998). The overall Gaussian shape of the differential scattering cross-section means that the scattering closely resembles the Boltzmann distribution for an equilibrium process. If the scattering did indeed resemble an equilibrium process, high- k (and therefore high-energy) scattering events would be very rare. The high- k tail in the scattering cross-sections increases the likelihood of such events happening significantly. Simulations show that, for both carbon and silicon, one electron in 10^6 imparts $k_B T$ or more energy to the atom at room temperature, $T = 300$ K. In our experiments, the fluence generally exceeds 10^8 electrons/nm² and so a significant number of high-energy interactions are to be expected. Events that do not break bonds will dissipate energy to the rest of the structure via acoustic waves, which presumably thermalize into phonons (heat). Some events will break bonds, damaging the structure and introducing long-range strain fields that permanently displace neighboring atoms. It appears likely that these are the events that are suppressing the variance signal.

CONCLUSIONS

Two important results have emerged from this study. The first is that the speckle statistics obtained in experimental FEM studies, in particular the normalized intensity variance, cannot be explained by kinematical electron scattering from a static model. Typically, the measured variance is about two orders of magnitude smaller than predicted in STFEM experiments at 200 kV, although the discrepancy can be reduced by an order of magnitude in DFFEM experiments (Borisenko et al., 2012). Although it was already known that strong variance suppression arises from spatial incoherence in the illumination, it was not so well appreciated that strong decoherence is also occurring.

Our simulations indicate that an important contribution to speckle suppression comes from displacement decoherence. Movements within the specimen give rise to rapid twinkling of the speckle pattern, which is then averaged over the exposure time needed for data acquisition. We show that the effect is equivalent to large atomic displacements, of the order of 0.1 nm or larger, presumably caused by beam interactions with the sample. The observed twinkling makes it clear that amorphous specimens are not structurally static under the beam. The diffraction data we collect is a time average over all of the structural configurations adopted by the sample as it adapts to the disruptions caused by the beam. Such large amplitudes of motion are comparable with typical bond distances and clearly cannot represent an equilibrium process. These disruptions are in addition to the thermal vibrations of the sample, which are much smaller in amplitude. Not all of these large motions need to be related to beam damage. Many displacements could be self-annealing if the atom does not move too far. A more realistic view of the specimen motion would be in terms of local regions tilting through small angles, in response to longer range stresses induced by beam damage events. This cooperative flexural mechanism, where significant numbers of atoms move together, can produce large temporal fluctuations in speckle intensity, analogous to Bragg reflections switching on and off from a small tilting crystal. Lowering the electron beam energy mitigates these decoherence effects considerably by reducing the beam damage rates.

Analogous to spatial incoherence (Treacy & Gibson, 1993), there is in effect a decoherence volume around each atom. In real specimens with beam damage occurring, atoms are not being displaced relative to some idealized model locations, such as lattice points in a crystal. It is the relative locations of atoms that matters. The further away that two atoms are, their temporal excursions in relative separation, $\Delta \mathbf{R}$, will also increase, probably diffusively as an accumulation of random walks, depending on what is happening to the material between them. A relative phase shift of $\mathbf{k} \cdot \Delta \mathbf{R} = \pm \pi/2$ is sufficient to disrupt interference, and the temporal fluctuations in phase shift will tend to grow in amplitude with increasing atom-pair separation. In this simple view, the decoherence volume is spherical and has that radius at which the average phase shift amplitude is large enough (i.e., $\pi/2$) to suppress constructive and destructive interferences.

A vivid analogy for displacement decoherence would be that, under the beam, the specimen behaves like a layer of

self-regenerating popcorn under a blowtorch flame; the irradiated atoms and their environs do not stay still during the exposure. Both the electron beam and recoiling atoms, are disrupting the sample, albeit transiently.

Multiple scattering in thicker samples also contributes to the suppression of variance, provided that the diffraction from successive sample layers can be considered mutually incoherent. Thus, multiple scattering in the presence of displacement decoherence further suppresses variance.

Energy-loss events, which randomize the phase of the scattered beam, are known to introduce decoherence (Howie, 2011). The phase randomization of the scattered wave is expected to suppress only the normalized variance peaks that arise from structurally ordered regions. In other words, only that speckle from ordered atomic arrangements is quenched, such as from local Bragg reflections. The normalized variance background, which arises from random atomic arrangements, is not affected by additional randomization.

Recently, it was argued that for samples under spatially incoherent illumination the normalized variance should depend on m and thickness t as

$$[mV(k) - 1]t = c, \quad (8)$$

where c is a constant and m was presumed constant (Treacy & Gibson, 2012). This expression was shown to hold under kinematical scattering conditions. It is now apparent that, with decoherence included, the effective value of m also changes with k . Our experiments on carbon show that the variation in $m(k)$ is less than a factor of 2 at 200 kV over the range $2 \leq k \leq 10 \text{ nm}^{-1}$. Clearly, this variation is sufficiently large to influence, but not necessarily invalidate, structural results from simulated annealing where it had been assumed that $m(k)$ is constant.

A second result emerged; the CRN model of amorphous silicon is not inconsistent with the experimental variance data if we allow for the effects of displacement decoherence and multiple scattering. This outcome may resolve the longstanding discrepancy between conclusions obtained from X-ray and electron diffraction studies of RDFs, and conclusions reached from previous FEM studies. RDF data is consistent with both the CRN and paracrystallite models because it cannot distinguish effectively between them. Earlier, FEM data had been thought to be more consistent with paracrystalline models, assuming that static kinematical theory was valid for emulating speckle. The present study reveals that decoherence mimics illumination spatial incoherence by suppressing random speckle. With decoherence included in the modeling, we now find that CRN models also produce normalized variance plots that broadly resemble experimental data. This suggests that (a) the paracrystalline length scale of $\sim 1.0\text{--}1.5 \text{ nm}$ previously claimed from FEM studies may be too long (Gibson et al., 1998), and that (b) the CRN model contains more MRO than was previously realized, as a random structure should show no normalized variance peaks. Paracrystallites are definitely present in most amorphous silicon samples, including well-annealed samples. Our results help explain why strong variance peaks are observed even though the fraction of paracrystallites is low, 5–15% being suggested by a recent study

(Borisenko et al., 2012; Treacy & Borisenko, 2012a, 2012b). It is now clear that the majority CRN phase is also contributing to the normalized variance peaks, albeit more weakly. This topic will be explored in a follow-up report.

Decoherence processes do not affect electron diffraction intensities from amorphous materials as strongly as they do the speckle, which may explain why the kinematical scattering approximation for electrons has enjoyed much success when describing diffraction with high-energy electron beams. In crystals, the diffuse intensity arising from sample tilts will be concentrated in the neighborhood of the main diffraction peaks. Nevertheless, decoherence is likely to present issues in studies involving quantitative imaging and diffraction.

Displacement decoherence is likely an important factor in electron ptychographical studies. Electron ptychography is closely related to FEM in that the data comprise a series of diffraction patterns from overlapping regions of the sample. Coherence in the data is crucial as speckle contains important medium- and long-range information. The strong effect of displacement decoherence may explain why electron ptychography works better at lower beam voltages (Kamimura et al., 2010; Humphry et al., 2012).

As our results with amorphous carbon and silicon confirm, the effects of beam damage can be mitigated by operation at lower beam voltage. Inherently, beam sensitive materials, such as polymers and biominerals, may require a different strategy such as collecting many low-dose nano-beam patterns from different areas, each area having received only a small electron fluence. Individual diffraction patterns will be dominated by shot noise. In principle, with a sufficiently large number of such patterns, the variance signal should emerge. FEM is inherently a statistical technique and the inability to make any strong statements about an individual diffraction pattern (or image pixel) is of no consequence to the technique. Such an approach will likely require low noise cameras.

Further, it seems clear that decoherence must be contributing to the so-called Stobbs factor, where experimental intensities of lattice images in high-resolution TEM are suppressed by factors of 3–8 relative to computed intensities (Hýtch & Stobbs, 1994; Boothroyd, 1998). Thermal scattering has been implicated previously as an important contribution to the Stobbs factor (Forbes et al., 2011). Displacement decoherence, although not thermal in origin, enhances the diffuse scattering significantly. The decoherence volume around each scatterer, from displacements and energy-loss events, will have an extent along the beam direction, L_D , that is generally less than the sample thickness, t , breaking each column effectively into $n \approx t/L_D$ mutually incoherent scattering lengths. n will be related to the m decoherence parameter, but we should keep in mind that it will depend on the Fourier components excited. Moreover, the detailed displacement mechanisms that drive displacement decoherence may well be different between crystals and amorphous polytypes. Each column of N atoms will have its coherent intensity contribution reduced by a factor of $N^2/[n \times (N/n)^2] = n$. A value of $n \approx 3$ –8 is sufficient to explain

the Stobbs factor in high-resolution TEM. As noted in this study, displacement decoherence depends on fluence, and possibly the fluence rate, and tends to be higher for STEM images where fluence rates are high.

When FEM was first introduced, the emphasis was predominantly on the experimental illumination conditions, and it was assumed that standard kinematical diffraction was sufficient to describe the scattering occurring from the (presumed static) structure, at least for those samples known to not damage appreciably under the beam. This study, and studies by others (Li et al., 2014), show that not only are the illumination and detection conditions important, but the details of the beam interaction with the sample also play a major role. It may not be possible to suppress beam damage completely in experiments. However, improved models of beam–sample interactions will likely improve our ability to simulate experimental FEM data, bringing FEM closer to being a fully quantitative technique.

ACKNOWLEDGMENTS

This research was supported by the US Department of Energy, Office of Basic Energy Sciences, Division of Materials Sciences and Engineering under Award DE-PS02-09ER09-01. The authors thank J.R. Abelson and B.S. Lee of the University of Illinois, Urbana-Champaign, and T. Sun and N. Zaluzec of Argonne National Laboratory, for providing the amorphous silicon sample. The authors are grateful to Murray Gibson, of Northeastern University, for many stimulating discussions.

REFERENCES

- ABRAMOWITZ, M. & STEGUN, I.A. (Eds.) (1965). *Handbook of Mathematical Functions*. Dover Publications: Mineola, New York.
- BARKEMA, G.T. & MOUSSEAU, N. (2000). High-quality continuous random networks. *Phys Rev B* **62**(8), 4985–4990.
- BISWAS, P., TAFEN, D. & DRABOLD, D.A. (2005). Experimentally constrained molecular relaxation: The case of GeSe₂. *Phys Rev B* **71**, 054204.
- BOGLE, S.N., VOYLES, P.M., KHARE, S.V. & ABELSON, J.R. (2007). Quantifying nanoscale order in amorphous materials: Simulating fluctuation electron microscopy of amorphous silicon. *J Phys Condens Matter* **19**(45), 455204.
- BOOTHROYD, C.B. (1998). Why don't high-resolution simulations and images match? *J Microsc* **190**(1–2), 99–108.
- BORISENKO, K.B., HABERL, B., CHEN, Y., LI, G., LIU, A., WILLIAMS, J.S., BRADBY, J.E., COCKAYNE, D.J.H. & TREACY, M.M.J. (2012). Medium-range order in amorphous silicon investigated by constrained structural relaxation of two-body and four-body electron diffraction data. *Acta Mater* **60**(1), 359–375.
- CHEN, L., CHENG, S., YU, C., SU, P., LIN, H. & CHI, K. (2002). Structural evolution in amorphous silicon and germanium thin films. *Microsc Microanal* **8**, 268–273.
- CHEN, X., SULLIVAN, J.P., FRIEDMANN, T.A. & GIBSON, J.M. (2004). Fluctuation microscopy studies of medium-range ordering in amorphous diamond-like carbon films. *Appl Phys Lett* **84**, 2823–2825.
- CHENG, J.-Y., TREACY, M.M.J., KEBLINSKI, P.J. & GIBSON, J.M. (2004). Diffraction microscopy for disordered tetrahedral networks. *J Appl Phys* **95**, 7779–7784.

- CHENG, S.L., LIN, H.H., HE, J.H., CHIANG, T.F., YU, C.H., CHEN, L.J., YANG, C.K., WU, D.Y., CHIEN, S.C. & CHEN, W.C. (2002). Evolution of structural order in germanium ion-implanted amorphous Si layers. *J Appl Phys* **92**, 910–913.
- COCKAYNE, D.J.H. (2007). The study of nanovolumes of amorphous materials using electron scattering. *Annu Rev Mater Res* **37**, 159–187.
- DAINTY, J.C. (1975). Stellar speckle interferometry. In *Laser Speckle and Related Phenomena*, Dainty, J.C. (Ed.), pp. 255–280). New York, NY: Springer-Verlag.
- DOYLE, P.A. & TURNER, P.S. (1968). Relativistic Hartree-Fock X-ray and electron scattering factors. *Acta Crystallogr A* **24**, 390–397.
- FAN, G.Y. & COWLEY, J.M. (1985). Autocorrelation analysis of high-resolution electron-micrographs of near-amorphous thin-films. *Ultramicroscopy* **17**, 345–355.
- FAN, G.Y. & COWLEY, J.M. (1988). Assessing the information-content of HREM images. *Ultramicroscopy* **24**, 49–60.
- FORBES, B., D'ALFONSO, A., FINDLAY, S., VAN DYCK, D., LEBEAU, J., STEMMER, S. & ALLEN, L. (2011). Thermal diffuse scattering in transmission electron microscopy. *Ultramicroscopy* **111**(12), 1670–1680.
- GIBBS, J.W. (1902). *Elementary Principles in Statistical Mechanics*. Mineola, New York: Dover Publications.
- GIBSON, J.M. (1978). Investigations of Amorphous Structures. PhD Thesis. Cambridge University, Cambridge, UK.
- GIBSON, J.M. & HOWIE, A. (1978). Investigation of local structure and composition in amorphous solids by high resolution electron microscopy. *Chem Scr* **14**, 109–116.
- GIBSON, J.M. & TREACY, M.M.J. (1997). Diminished medium-range order observed in annealed amorphous germanium. *Phys Rev Lett* **78**, 1074–1077.
- GIBSON, J.M., TREACY, M.M.J., SUN, T. & ZALUZEC, N.J. (2010). Substantial crystalline topology in amorphous silicon. *Phys Rev Lett* **105**(12), 125504.
- GIBSON, J.M., TREACY, M.M.J., VOYLES, P.M., JIN, H.-C. & ABELSON, J.R. (1998). Structural disorder induced in hydrogenated amorphous silicon by light soaking. *Appl Phys Lett* **73**, 3093–3096.
- GOODMAN, J. (1975a). Probability density function of the sum of n partially correlated speckle patterns. *Opt Commun* **13**(3), 244–247.
- GOODMAN, J.W. (1975b). Some fundamental properties of speckle. In *Laser Speckle and Related Phenomena*, Dainty, J.C. (Ed.), pp. 60–68). New York, NY: Springer-Verlag.
- HIRSCH, P., HOWIE, A., NICHOLSON, R., PASHLEY, D.W. & WHELAN, M.J. (1977). *Electron Microscopy of Thin Crystals*. Malabar, FL: Krieger Publishing.
- HOWIE, A. (1978). High resolution electron microscopy of amorphous thin films. *J Non Cryst Solids* **31**, 41–45.
- HOWIE, A. (2011). Mechanisms of decoherence in electron microscopy. *Ultramicroscopy* **111**(7), 761–767.
- HOWIE, A., KRIVANEK, O.L. & RUDEE, M.L. (1973). Interpretation of electron micrographs and diffraction patterns of amorphous materials. *Philos Mag* **27**, 235–255.
- HOWIE, A., MCGILL, C.A. & RODENBURG, J.M. (1985). Intensity correlations in microdiffraction from amorphous materials. *J Phys Colloques* **46**, C9-59–C9-62.
- HUMPHRY, M.J., KRAUS, B., HURST, A.C., MAIDEN, M. & RODENBURG, J.M. (2012). Ptychographic electron microscopy using high-angle dark-field scattering for sub-nanometre resolution imaging. *Nat Commun* **3**, 730.
- HWANG, J., CLAUSEN, A.M., CAO, H. & VOYLES, P.M. (2009). Reverse monte carlo structural model for a zirconium-based metallic glass incorporating fluctuation microscopy medium-range order data. *J Mater Res* **24**(10), 3121–3129.
- HÛTCH, M. & STOBBS, W. (1994). Quantitative comparison of high resolution TEM images with image simulations. *Ultramicroscopy* **53**(3), 191–203.
- JAYNES, E.T. (1957). Information theory and statistical mechanics. *Phys Rev* **106**, 620–630.
- KAMIMURA, O., DOBASHI, T., KAWAHARA, K., ABE, T. & GOHARA, K. (2010). 10-kv diffractive imaging using newly developed electron diffraction microscope. *Ultramicroscopy* **110**(2), 130–133.
- KAPUR, J.N. (1989). *Maximum-Entropy Models in Science and Engineering*. New Delhi, India: New Age International Publishers.
- KEBLINSKI, P., PHILLIPOT, S., WOLF, D. & GLEITER, H. (1997). Amorphous structure of grain boundaries and grain junctions in nanocrystalline silicon by molecular-dynamics simulation. *Acta Mater* **45**(3), 987–998.
- KIRKLAND, E.J. (1998). *Advanced Computing in Electron Microscopy*. New York, NY and London: Plenum Press.
- LAAZIRI, K., KYCIA, S., ROORDA, S., CHICOINE, M., ROBERTSON, J.L., WANG, J. & MOSS, S.C. (1999). High-energy x-ray diffraction study of pure amorphous silicon. *Phys Rev B* **60**(19), 13520–13533.
- LEE, B.-S., BISHOP, S.G. & ABELSON, J.R. (2010). Fluctuation transmission electron microscopy: Detecting nanoscale order in disordered structures. *Chemphyschem* **11**, 2311–2317.
- LI, J., GU, X. & HUFNAGEL, T.C. (2001). Medium-range order in metallic glasses studied by fluctuation microscopy. *Microsc Microanal* **7**(Suppl 2), 1260–1261.
- LI, J., GU, X. & HUFNAGEL, T.C. (2003). Using fluctuation microscopy to characterize structural order in metallic glass. *Microsc Microanal* **9**, 509–515.
- LI, T.T., BOGLE, S.N. & ABELSON, J.R. (2014). Quantitative fluctuation electron microscopy in the stem: Methods to identify, avoid, and correct for artifacts. *Microsc Microanal* **20**, 1605–1618.
- LI, T.T., DARMAWIKARTA, K. & ABELSON, J.R. (2013). Quantifying nanoscale order in amorphous materials via scattering covariance in fluctuation electron microscopy. *Ultramicroscopy* **133**, 95–100.
- LIU, A.C.Y., ARENAL, R., MILLER, D.J., CHEN, X., JOHNSON, J.A., ERYILMAZ, O.L., ERDEMIR, A. & WOODFORD, J.B. (2007). Structural order in near-frictionless hydrogenated diamond like carbon films probed at three length scales via transmission electron microscopy. *Phys Rev B* **75**, 205402.
- MCBRIDE, W. & COCKAYNE, D.J.H. (2003). The structure of nanovolumes of amorphous materials. *J Non Cryst Solids* **318**, 233–238.
- PRESS, W.H., TEUKOLSKY, S.A., VETTERLING, W.T. & FLANNERY, B.P. (1992). *Numerical Recipes in C; the Art of Scientific Computing*, 2nd ed Cambridge, UK: Cambridge University Press.
- RODENBURG, J.M. (1988). Properties of electron microdiffraction patterns from amorphous materials. *Ultramicroscopy* **25**, 329–344.
- RODENBURG, J.M. (2008). Ptychography and related diffracted imaging methods. In *Advances in Imaging and Electron Physics* (vol. 150 Hawkes, P.W. (Ed.), pp. 87–184). Amsterdam, Netherlands: Elsevier.
- STRATTON, W.G., HAMANN, J., PEREPEZKO, J.H., VOYLES, P.M., KHARE, S.V. & MAO, X. (2005). Aluminum nanoscale order in amorphous Al₉₂Sm₈ measured by fluctuation electron microscopy. *Appl Phys Lett* **86**, 141910.
- STRATTON, W.G. & VOYLES, P.M. (2008). A phenomenological model of fluctuation electron microscopy for a nanocrystal/amorphous composite. *Ultramicroscopy* **108**(8), 727–736.
- SUN, T., KOECK, F.A.M., REZIKYAN, A., TREACY, M.M.J. & NEMANICH, R.J. (2014). Thermally enhanced photoinduced electron emission from nitrogen-doped diamond films on silicon substrates. *Phys Rev B* **90**, 121302.

- TREACY, M. & GIBSON, J. (2012). Examination of a polycrystalline thin-film model to explore the relation between probe size and structural correlation length in fluctuation electron microscopy. *Microsc Microanal* **18**, 241–253.
- TREACY, M.M.J. (2005). What is fluctuation microscopy? *Microsc Today* **13**(5), 20–21.
- TREACY, M.M.J. (2012). Speckles in images and diffraction patterns. In *Handbook of Nanoscscopy* (chapter 12 van Tendeloo, G., van Dyck, D. & Pennycook, S.J. (Eds.), pp. 405–435). Hoboken, New Jersey, USA: John Wiley and Sons.
- TREACY, M.M.J. & BORISENKO, K.B. (2012a). The local structure of amorphous silicon. *Science* **335**(6071), 950–953.
- TREACY, M.M.J. & BORISENKO, K.B. (2012b). Response to comment on local structure of amorphous silicon. *Science* **338**(6114), 1539.
- TREACY, M.M.J. & GIBSON, J.M. (1993). Coherence and multiple scattering in “Z”-contrast images. *Ultramicroscopy* **52**, 31.
- TREACY, M.M.J. & GIBSON, J.M. (1996). Variable coherence microscopy: A rich source of structural information from disordered materials. *Acta Cryst A* **52**, 212–220.
- TREACY, M.M.J., GIBSON, J.M., FAN, L., PATERSON, D.J. & McNULTY, I. (2005). Fluctuation microscopy: A probe of medium range order. *Rep Prog Phys* **68**(12), 2899–2944.
- TREACY, M.M.J., GIBSON, J.M. & KEBLINSKI, P.J. (1998). Paracrystallites found in evaporated amorphous tetrahedral semiconductors. *J Non Cryst Solids* **231**, 99–110.
- VOYLES, P.M. & ABELSON, J.R. (2003). Medium-range order in amorphous silicon measured by fluctuation electron microscopy. *Sol Energy Mater Sol Cells* **78**, 85–113.
- VOYLES, P.M., GERBI, J.E., TREACY, M.M.J., GIBSON, J.M. & ABELSON, J. R. (2001). Increased medium-range order in amorphous silicon with increased substrate temperature. *Phys Rev Lett* **86**, 5514–5518.
- WEN, J., CHENG, Y.Q., WANG, J.Q. & MA, E. (2009). Distinguishing medium-range order in metallic glasses using fluctuation electron microscopy: A theoretical study using atomic models. *J Appl Phys* **105**, 043519.
- WOOTEN, F., WINER, K. & WEAIRE, D. (1985). Computer-generation of structural models of amorphous Si and Ge. *Phys Rev Lett* **54**, 1392–1395.
- XIE, R., LONG, G.G., WEIGAND, S.J., MOSS, S.C., CARVALHO, T., ROORDA, S., HEJNA, M., TORQUATO, S. & STEINHARDT, P.J. (2013). Hyperuniformity in amorphous silicon based on the measurement of the infinite-wavelength limit of the structure factor. *Proc Natl Acad Sci USA* **110**, 13250–13254.
- ZHAO, G., BUSECK, P.R., ROUGÉE, A. & TREACY, M.M.J. (2009). Medium-range order in molecular materials: Fluctuation electron microscopy for detecting fullerenes in disordered carbons. *Ultramicroscopy* **109**, 177–188.
- ZHAO, G., TREACY, M.M.J. & BUSECK, P.R. (2010). Fluctuation electron microscopy of medium-range order in ion-irradiated zircon. *Philos Mag* **90**(35), 4661–4677.

APPENDICES

Phenomenological explanations for negative exponential, and Gamma distribution, statistics have been presented in an earlier publication (Treacy, 2012). Here, we present justifications based on information theory.

Full Spatial Coherence: Negative Exponential Speckle Statistics

We seek the most likely pixel intensity distribution, $P(I)$, in an image where each pixel intensity is random and uncorrelated with its neighbors. Our approach is based on the maximum informational entropy method of Jaynes (Jaynes, 1957; Kapur, 1989). Boltzmann and Gibbs used a related thermodynamical argument to obtain the distribution of energy states in a system that is in thermodynamic equilibrium—the Boltzmann distribution—which is also a negative exponential (Gibbs, 1902).

There are two constraints applied to the system. The first is that the probability distribution be normalized. Treating intensity as a continuous variable, this means that

$$\int_0^{\infty} P(I) dI = 1. \quad (\text{A.1})$$

The second constraint is that the distribution must preserve the mean intensity, $\langle I \rangle$

$$\int_0^{\infty} I P(I) dI = \langle I \rangle. \quad (\text{A.2})$$

This is equivalent to conserving the total number of electrons within the electron micrograph.

The informational entropy of such a distribution is (Jaynes, 1957)

$$S = - \int_0^{\infty} P(I) \ln(P(I)) dI. \quad (\text{A.3})$$

The most likely distribution is found by maximizing the informational entropy under the two constraints. This is done by rewriting the entropy as

$$S' = - \int_0^{\infty} P(I) \ln(P(I)) dI + \lambda_1 \left(\int_0^{\infty} P(I) dI - 1 \right) + \lambda_2 \left(\int_0^{\infty} I P(I) dI - \langle I \rangle \right). \quad (\text{A.4})$$

λ_1 and λ_2 are Lagrange multipliers. The entities in large brackets are 0 if the constraints hold true, and so $S' = S$ under those conditions.

At maximum (or minimum) entropy, we must have

$$\frac{\partial S'}{\partial P} = \int_0^{\infty} [-\ln(P(I)) + 1 + \lambda_1 + \lambda_2 I] dI = 0. \quad (\text{A.5})$$

This must hold true over the whole range of $P(I)$ values, and so we can assert that

$$-\ln P(I) + 1 + \lambda_1 + \lambda_2 I = 0, \quad (\text{A.6})$$

which gives, upon taking the antilogarithm,

$$P(I) = A \exp(\lambda_2 I), \quad (\text{A.7})$$

where the constant $A = \exp(1 + \lambda_1)$. Applying the constraints (A.1) and (A.2), we solve for A and λ_2 to obtain

$$P(I) = \frac{1}{\langle I \rangle} \exp\left(-\frac{I}{\langle I \rangle}\right), \quad (\text{A.8})$$

which is a negative exponential distribution. Taking the second derivative of (A.5) gives

$$\frac{\partial^2 S'}{\partial P^2} = - \int_0^\infty \frac{dI}{P(I)} = - \langle I \rangle \int_0^\infty \exp\left(\frac{I}{\langle I \rangle}\right) dI \rightarrow -\infty,$$

confirming that the negative exponential distribution (A.8) gives the maximum informational entropy, and is therefore the most likely distribution of intensity when the mean intensity is fixed.

Clearly, there is only one arrangement possible where the intensity is exactly $\langle I \rangle$ in every pixel. There are vastly more ($\sim e^S$) distinct negative exponential-type distributions, which give the same mean, than there are any other type of distribution.

Partial Spatial Coherence: Gamma Distribution Speckle Statistics

Goodman (1975a, 1975b) showed that partially coherent laser speckle should exhibit Gamma distribution speckle statistics. His matrix approach is different to both the information-theoretic derivation presented here, and our earlier phenomenological explanation (Treacy, 2012).

We desire the most probable normalized intensity distribution, $P(I)$, when the mean intensity $\langle I \rangle$ is fixed and also when the effective number of mutually incoherent sources, m , is fixed. As before, the normalization and mean constraints are given by (A.1) and (A.2), respectively. Although it is not obvious at this juncture, the constraint on the m parameter is most conveniently imposed by holding the geometric mean of the intensity, g , constant. The geometric mean of a distribution of n values of I_i is determined from the $1/n$ th power of the product of the n values of I_i

$$g = \left(\prod_{i=1}^n I_i \right)^{\frac{1}{n}}.$$

Taking the logarithm converts this product into a sum

$$\ln g = \frac{1}{n} \sum_{i=1}^n \ln(I_i), \tag{A.9}$$

and so the geometric mean can be expressed as

$$g = \exp\left(\frac{1}{n} \sum_{i=1}^n \ln(I_i)\right).$$

If g is constrained, then so is $\ln(g)$, and (A.9) is a convenient mathematical form for the constraint—to hold $\ln(g)$ constant. In the limit as $n \rightarrow \infty$, the sum, divided by n , converts into an integral, thus the third constraint on $P(I)$ is equivalent to fixing

$$\ln g = \int_0^\infty \ln(I) P(I) dI. \tag{A.10}$$

The fact that this is equivalent to a constraint on m will emerge later.

The modified informational entropy, S' , can be expressed now with three Lagrange multipliers, λ_1, λ_2 , and λ_3

$$S' = - \int_0^\infty P(I) \ln(P(I)) dI + \lambda_1 \left(\int_0^\infty P(I) dI - 1 \right) + \lambda_2 \left(\int_0^\infty IP(I) dI - \langle I \rangle \right) + \lambda_3 \left(\int_0^\infty \ln(I) P(I) dI - \ln g \right). \tag{A.11}$$

This equals the informational entropy, S , if the three constraints hold true. The entropy is maximized (or minimized) if

$$\frac{\partial S'}{\partial P} = \int_0^\infty [-\ln(P(I)) + 1 + \lambda_1 + \lambda_2 I + \lambda_3 \ln(I)] dI = 0. \tag{A.12}$$

This requires

$$-\ln(P(I)) + 1 + \lambda_1 + \lambda_2 I + \lambda_3 \ln(I) = 0,$$

for all I , and so

$$P(I) = AI^{\lambda_3} \exp(\lambda_2 I), \tag{A.13}$$

where $A = \exp(1 + \lambda_1)$. The three constants, A, λ_2 and λ_3 are obtained by applying the three constraints (A.1), (A.2), and (A.10). The constraint integrals can be evaluated by noting that

$$\int_0^\infty x^{n-1} \exp(-ax) dx = \frac{\Gamma(n)}{a^n},$$

$$\int_0^\infty x^{n-1} \exp(-ax) \ln(x) dx = \frac{d}{dn} \left[\int_0^\infty x^{n-1} \exp(-ax) dx \right] = \frac{1}{\Gamma(n)} \frac{d\Gamma(n)}{dn} - \ln(a), \tag{A.14}$$

where $\Gamma(n)$ is the Gamma function.

Solving gives

$$\lambda_2 = - \frac{\lambda_3 + 1}{\langle I \rangle}; \quad A = \frac{1}{\langle I \rangle^{\lambda_3 + 1} \Gamma(\lambda_3 + 1)}.$$

If we set $\lambda_3 + 1 = m$, then we obtain the familiar form of the Gamma distribution

$$P(I) = \frac{m^m}{\Gamma(m)} \frac{I^{m-1}}{\langle I \rangle^m} \exp\left(-\frac{mI}{\langle I \rangle}\right). \tag{A.15}$$

Differentiating (A.12) again confirms that this is the most likely distribution.

We find that for the geometric mean, g , using the standard integrals (A.14)

$$\ln(g) = \frac{1}{\Gamma(m)} \frac{d\Gamma(m)}{dm} + \ln\left(\frac{\langle I \rangle}{m}\right),$$

which depends on m and $\langle I \rangle$ only. As the mean $\langle I \rangle$ is already constrained, the constraint on the geometric mean, g , is then equivalent to constraining m , as claimed earlier. Tables of both the Gamma function, $\Gamma(m)$, and the Digamma function, $\psi(m) = \frac{1}{\Gamma(m)} \frac{d\Gamma(m)}{dm}$, are available (Abramowitz & Stegun, 1965).

The Gamma distribution is the least biased normalized distribution when both the mean, $\langle I \rangle$, and the variance, $\langle I \rangle^2/m$ (or, the normalized variance, $V = 1/m$), are fixed.